University of Alberta

Pressure Gradients and Annealing Effects in Solid Helium-4

by

Md. Abdul Halim Suhel

A thesis submitted to the Faculty of Graduate Studies and Research
in partial fulfillment of the requirements for the degree of

Master of Science

Department of Physics

Spring 2011
Edmonton, Alberta

This thesis is dedicated to my parents, **Abdul Matin** and **Sujya Khanom**.

Abstract

The Kim and Chan experiment in 2004 gave the first experimental evidence of a possible supersolid state. Even though the origin of this state is not clear yet, several experimental and theoretical investigations suggest defects are responsible for this curious phase. We have used heat pulses and thermal quenching to study pressure gradients and annealing mechanisms in solid ^{4}He crystals. Large pressure gradients exist in crystals grown at constant volume. These can be enhanced by phase transitions, thermal quenching or by partial melting. Annealing reduces defect densities and hence pressure gradients in crystals. Our measurements show that the pressure at different points in a crystal can behave differently, even if there is little change in the crystal's average pressure. We measured the activation energy that is associated with the annealing process.

Acknowledgements

I would like to express my sincere gratitude to my supervisor, John Beamish for his constant support and encouragement during my research works. My special thanks goes to Alex Syshchenko, who taught me the techniques of doing experiments in Low temperature physics. He was always there to help me with his precious advices when I needed it most.

Lots of appreciation for the valuable help of Steve Rogers, Tony Walford, Don Mullin and Sarah Derr, they were always very cooperative. I am very grateful to all my family and friends for their inspirations.

Table of Contents

List of Tables

List of Figures

List of symbols

Λ	De Boer parameter
V(r)	Lennard-Jones Potential
γ	Gruneisen Parameter
A_{Debye}	Coefficient of cubic term in heat capacity
B_{TLS}	Coefficient of linear term in heat capacity
γ_{Debye}	Debye contribution to Gruneisen parameter
γ_{TLS}	TLS system contribution to Gruneisen parameter
κ	Rate of thermal process
τ	Thermal time constant
E	Thermal activation energy

Chapter 1

Introduction

Helium is the most peculiar of all materials. It remains liquid under its saturated vapor pressure. Even at absolute zero temperature, helium can only be solidified under an external pressure of 25 bar or more. This, and the many curious properties displayed by this strange material, make it a very appealing research subject.

Solid ^{4}He is an intense subject of study because of its quantum nature. After the observation of superfluidity in liquid ^{4}He, a similar type of transition was predicted in solid ^{4}He. After a number of experimental approaches, an experiment in 2004 [1] finally revealed evidence of decoupling of solid ^{4}He from torsional oscillations at a temperature around 200 mK. This decoupling was inferred from a drop in oscillation period. Flow of mass in solid ^{4}He crystals was detected in a later experiment in 2009 [2], but the temperature range where this flow was observed was different from that of the decoupling. Also, a shear modulus measurement in 2007 [3] showed large stiffening in solid ^{4}He which occurred in the same temperature range as the decoupling.

These phenomena are unusual for a solid and some of them are indeed similar to the superfluid properties of liquid ^{4}He. This strengthens the early idea of some theorists [4, 5] that there might be a phase transition in solid ^{4}He too. This

proposed state is termed a "supersolid". However, experimentally the behavior is found to be greatly dependent on the impurity concentration, sample history, annealing, cell geometry, etc. This raises the issue that the observed characteristics might not be intrinsic properties of perfect crystals. Several experiments suggest the existence of a glassy phase [6, 7] at low temperatures that might be related to the unusual phenomena. A superglass [8] phase has been proposed based on torsional oscillator relaxation measurements. Various theories have been developed to explain the experimental observations. Most suggest that the observed results are not intrinsic properties of ^{4}He crystal, but rather are introduced by defects, although one theory considers supersolidity to be an intrinsic property of ^{4}He crystal [9], with defects only enhancing those properties.

Despite many efforts, the properties and origin of a possible supersolid phase in solid ^{4}He are still not clear. This thesis is an attempt to study the characteristics of solid ^{4}He crystal by means of pressure-temperature measurements. Plastic deformation of crystal was used to create pressure gradients and defects. Crystals were annealed both at high and low temperature to see the effect on pressure gradients. The temperature dependence of the annealing process, as seen in pressure changes, was used to try to identify the annealing mechanism. The presence of a T^2 (glass) term in a system's pressure is often associated with glasses and this thesis reports on attempts to see such a term in solid ^{4}He. The objective of all these measurements is to obtain information about the behavior of disorder (defects) in solid ^{4}He crystals, including their relationship to a possible supersolid state.

The thesis is organized as follows. Chapter 2 gives brief information about the properties of solid ^{4}He along with discussion of defects and their contribution to the characteristics of solid ^{4}He. Chapter 3 describes the design and techniques of the experiment, including semi-quantitative calculations of thermal and mechanical parameters. Chapter 4 presents our experimental results and discussion. Finally, Chapter 5 summarizes the thesis.

Chapter 2

Background

This chapter will discuss the properties of solid ^{4}He, including its quantum and supersolid nature. This will be followed by more detailed information about supersolidity and its dependence on crystal defects. Finally, information about pressure and its relationship to other characteristics of solid ^{4}He will be provided.

2.1 Properties of Helium

Helium is the second most abundant element in the universe just after hydrogen. Physically it is an odorless, colorless, tasteless, light inert gas. It is the smallest of all atoms with an atomic radius of 31 pm [10]. Some of its other properties are: zero permanent electric dipole moment, weak diamagnetic susceptibility, the smallest known atomic polarizability and the highest ionization energy of 24.6 eV [10].

The normal boiling point of ^{4}He is 4.2 K. At this temperature, it is a regular liquid exhibiting small viscosity. However, everything changes when its temperature reaches 2.17 K; there it undergoes a second order phase transition with a large anomalous behavior in specific heat. This behavior is named the 'lambda' (λ) anomaly and it marks a very significant transition to a new phase of matter, the "superfluid" phase. The features of this phase cannot be explained by classical mechanics. It requires a quantum mechanical approach and involves a

fraction of the atoms undergoing Bose-Einstein condensation (BEC). Some of the characteristics of this superfluid phase are: fountain effect, second sound, third sound, fourth sound, quantum vortices, non-classical rotational inertia (NCRI) etc.

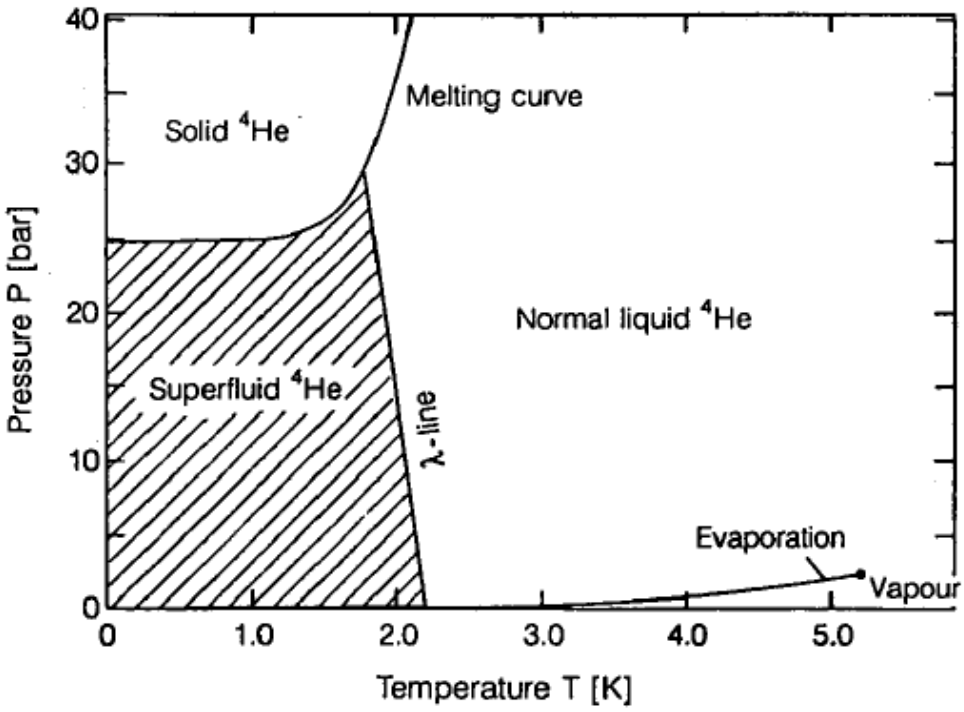

Figure 2.1: Phase diagram of ^{4}He with the solid and liquid region marked. Taken from [11].

^{4}He can only be solidified by applying an external pressure of at least 25 bar (Figure 2.1). Its reluctance to solidify under its own vapor pressure originates from the weak binding forces between the atoms and the large non-thermal quantum mechanical zero point energy. The weak binding force arises due to the closed electronic shell and the zero point energy comes from its low atomic mass.

A parameter which quantifies the quantum nature of solid helium is the dimensionless De Boer parameter (Λ). It is defined as the ratio of zero point energy to the potential energy

$$\Lambda = \frac{h}{\sigma\sqrt{m\varepsilon}} \tag{2.1}$$

where $h, \sigma, m, \varepsilon$ are respectively Planck's constant, the range of interaction, the mass of the atom and strength of the interaction. The range and strength of the interaction can be obtained from the Lennard-Jones potential

$$V(r) = 4\varepsilon[(\frac{\sigma}{r})^{12} - (\frac{\sigma}{r})^{6}] \tag{2.2}$$

As shown in Table 2.1, the most quantum crystal in nature is ^{3}He (Λ=3.01) followed by ^{4}He (Λ=2.61). Since ^{3}He has spin 1/2, the best candidate to study phenomena like Bose condensation is ^{4}He.

gas	ϵ (K)	σ (nm)	m (amu)	Λ
Xe	230.4	0.392	131.30	0.064
Kr	164.0	0.362	83.80	0.103
Ar	119.8	0.340	39.944	0.186
Ne	36.7	0.279	20.183	0.577
^{4}He	10.2	0.262	4.004	2.61
^{3}He	10.2	0.262	3.017	3.01

Table 2.1: De Boer parameter for the inert gas solids [12]. ^{3}He is the most quantum solid.

2.2 Characteristics of supersolid

Supersolidity is the phenomena of solid flowing without viscous dissipation, i.e., the solid acts as a solid as well as a superfluid. The first experimental evidence for such a supersolid phase was found in a torsional oscillator experiment where non-classical rotational inertia (NCRI) was observed in solid ^{4}He [1]. As the temperature of a solid ^{4}He crystal was lowered, its moment of inertia started dropping at temperature around 200 mK, which is unusual in the case of solid. This odd behavior is termed as non-classical rotational inertia (NCRI). However, the existence of such a phase was predicted in the early seventies, including theories [4] based on point defects like vacancies. Recent theories are based on the idea that the observed supersolid effects depend on crystal defects such as dislocations [13], grain boundaries [14] or existence of glassy regions [15].

Though the origin of this supersolid phase has yet to be determined, several experiments have shown unusual behavior which may be related to a supersolid phase, including mass flow [2], NCRI [1] and shear stiffening [3]. The proposed supersolid phase (Figure 2.2) is identified by a separate region in the solid phase of the ^{4}He phase diagram. The first evidence for this supersolid phase came from a pioneering torsional oscillator experiment [1] by Kim & Chan. A torsional oscillator containing solid ^{4}He in vycor was driven by an AC voltage and the frequency of oscillation was recorded. Then the torsional oscillator was cooled and when the temperature reached 200 mK, the frequency of oscillation began to rise giving a drop in oscillation period. This rise in frequency suggests some solid ^{4}He decoupled from oscillation at that temperature and hence probable

supersolidity. The Kim and Chan data for a similar measurement in bulk solid ^{4}He [16] is shown in Figure 2.3(A). Figure 2.3(B) also shows similar measurement in the case of a crystal grown in a blocked annular cell with the expected reduction in resonant period drop.

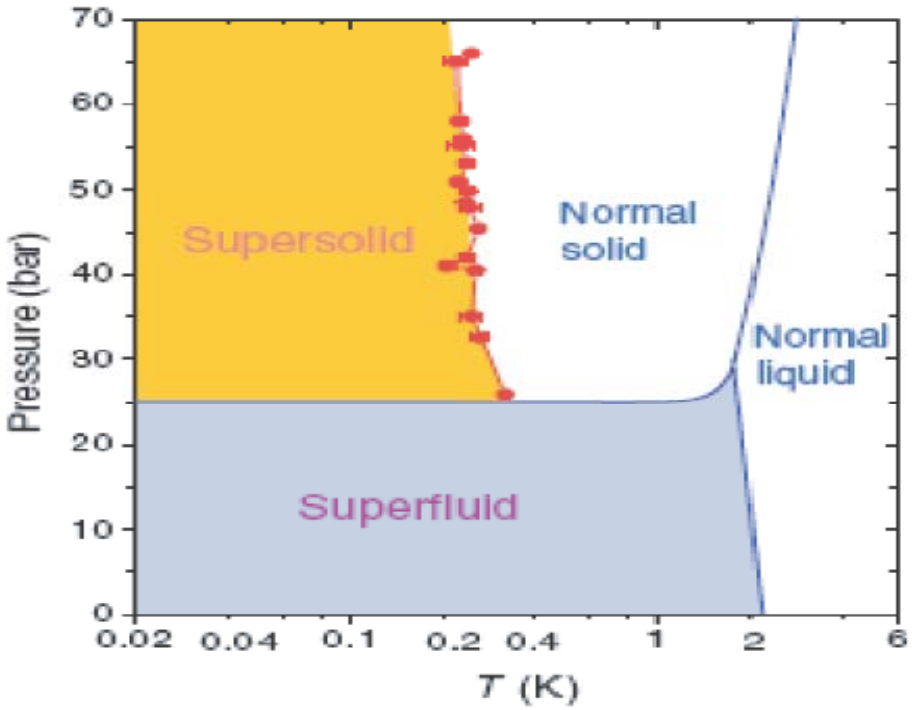

Figure 2.2: Phase diagram of ^{4}He with the clear indication of the supersolid phase. Taken from [16].

Unusual behavior was also observed in a shear modulus experiment [3] by Day & Beamish. A rise in shear modulus (Figure 2.4) was seen in the same temperature range of the observed NCRI. This rise was interpreted as stiffening of solid ^{4}He due to the pinning of dislocations in this temperature range. The NCRI and the shear stiffening show that something is happening in solid ^{4}He in this temperature range, which may be supersolidity.

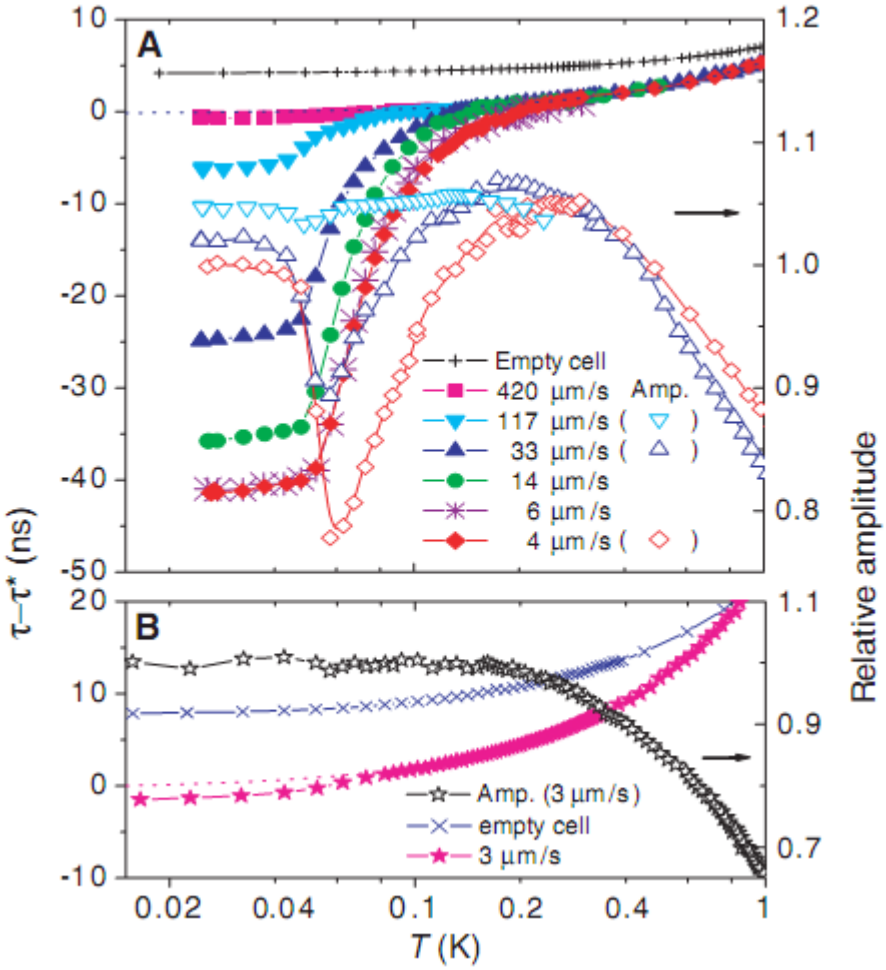

Figure 2.3: (A) Resonant period and oscillation amplitude are plotted as a function of temperature for a 51 bar solid ^{4}He crystal at different maximum oscillation velocities in an open cell. (B) Similar resonant period and oscillation amplitude measurement for a 36 bar crystal in a blocked annular cell. The dotted line in both plots represents the period shift of the empty cell. The blocking in the cell strongly reduced the period shift in comparison to the unblocked cell. Taken from [16].

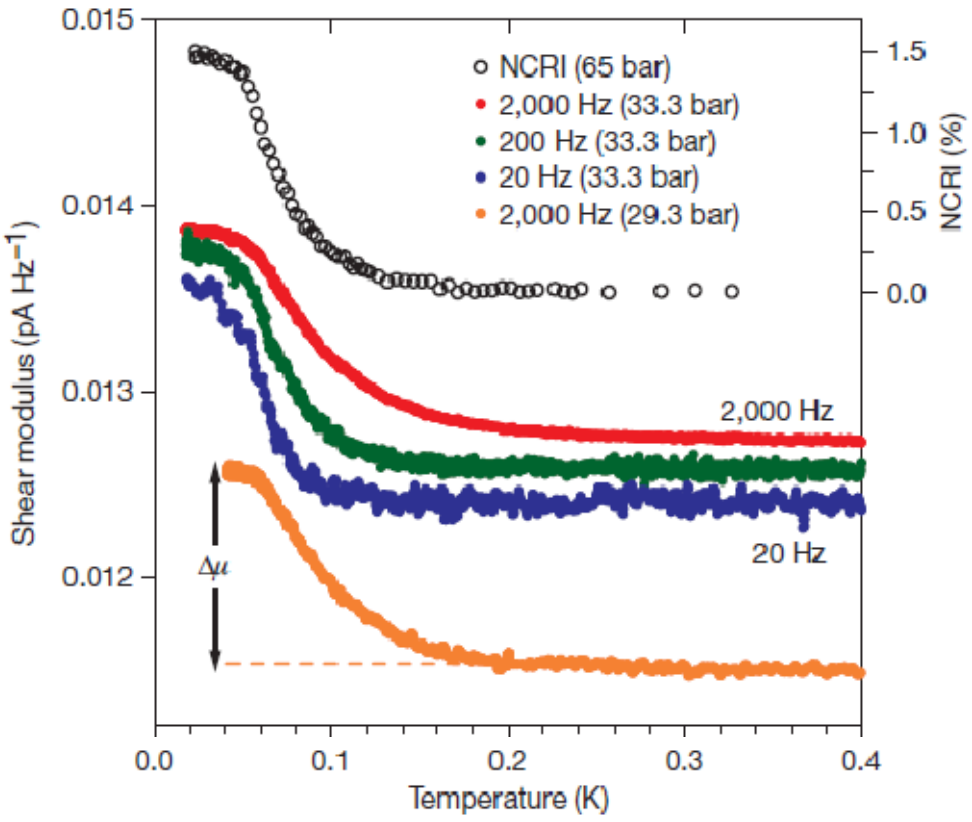

Figure 2.4: Shear modulus of solid ^{4}He at strain 2.2×10^{-8} is plotted as a function of temperature. Shear modulus is given as I/f, where I is the measured current and f is the frequency; data have been offset for clarity. Shear modulus at different frequencies is illustrated by different plots. Taken from [3].

2.3 Supersolidity and perfect crystal

This apparent supersolid behavior is observed only in the case of solid ^{4}He [1]. Whether it can exist in a perfect ^{4}He crystal is still questionable. The NCRI is found to be related to the crystal quality. A large NCRI fraction (NCRIf) is exhibited in a disordered crystal but the NCRIf goes down in annealed crystals and sometimes it disappears [17]. Defects like grain boundaries [18] can produce superfluid like behavior of solid ^{4}He. Based on experimental observation and a number of theoretical studies, many researchers have concluded that supersolidity

cannot exist in a perfect commensurate [19] crystal and that defects are responsible for the observed phenomena.

2.4 Roles of defects in supersolidity

Defects are believed to play a significant role in supersolidity of ^{4}He crystals, based on theoretical and experimental observations. Crystals can contain point defects and higher dimensional defects. Point defects like vacancies [4] and interstitials [20] are introduced thermally or by zero point motion in ^{4}He crystals, in which case they might become delocalized and undergo a BEC transition, giving rise to supersolid behavior. Defects like ^{3}He impurities contribute to the anomalous behavior observed in solid ^{4}He [21]. Dislocations are higher dimensional defects that appear to be responsible for the unusual elastic behavior in solid ^{4}He [3] and perhaps for the supersolid response in torsional oscillators [22]. Interaction between defects can also be important. For example, ^{3}He impurities can pin dislocations in solid ^{4}He. Dislocations can form grain boundaries which have been associated with dc mass flow in ^{4}He crystals [18] although later measurements [23] showed that the flow was in liquid channels at the edges of grain boundaries. The possibility of a few atomic layers of grain boundaries becoming supersolid was also considered in another flow experiment [24]. Thus information about defects like vacancies, interstitials, impurities, dislocations and grain boundaries is important in understanding the probable supersolid behavior of solid ^{4}He.

2.5 Stress and defects

In a perfect crystal there are no defects whereas large numbers of defects will be found in disordered crystals. Applying stress introduces deformation in a crystal. Deformation can be elastic or plastic depending on the amount of stress being applied. Elastic deformation is reversible, i.e., the crystal regains its original shape after the stress is removed. Plastic deformation occurs when the applied stress exceeds a threshold called the yield stress. After plastic deformation [25] the crystal becomes permanently distorted, and large numbers of defects are produced, particularly dislocations.

To study supersolidity and its dependence on defects we need to create defects by applying stresses. This can be done by using the blocked capillary method to grow crystals. This is a constant volume method in which blocking the capillary causes the crystal to grow at constant density. The large pressure drop along the melting curve deforms the crystal during cooling and produces a large pressure gradient (∇P) in it. A crystal can also be stressed by sudden temperature change. This can be done by applying heat pulses to the crystal. A temperature gradient (∇T) produced by heat pulses thermally expands the crystal, which creates a pressure gradient and causes plastic deformation. Even larger pressure changes (ΔP) can be introduced by melting part of the crystal followed by quench cooling to re-crystallize it.

Annealing is a well known procedure to remove crystal defects. When a crystal is warmed up near to the melting temperature, redistribution of the atoms

takes place by thermally activated processes, often involving vacancies. This rearrangement of atoms eliminates some crystal defects. More defects can be annealed away if the crystal is kept at a temperature close to melting for a longer period. Thus, defects can be created in a crystal by deforming it and most of them can be removed by annealing.

2.6 Stress pressure relationship

A pressure gradient in a crystal is a measure of stress (σ) in it. Stress is defined as the force (F) per unit area (A) acting on a surface.

$$\sigma = \frac{F}{A} \tag{2.3}$$

If the force is perpendicular to the surface, this is just the pressure (P). If it is parallel to the surface it is the shear stress. The relation between stress and pressure gradient in a solid can be illustrated by assuming a cylindrical cell (Figure 2.5) containing solid helium.

Let us assume the cylinder is long compared to its radius [L>>R] and has a pressure difference ΔP between its two opposite ends. The two forces acting on a short length of the helium cylinder are due to the pressure on its cross sectional area πR^2 and the force in the opposite direction due to the stress at the cylinder's wall. We assume the stress to be uniform along the cylinder's surface. Then, for a cylinder of length L, the stress is given by

$$\sigma = \frac{F}{2\pi RL} \tag{2.4}$$

where F is the force due to the difference in pressure at the two ends:

$$F = \pi R^2 \Delta P \tag{2.5}$$

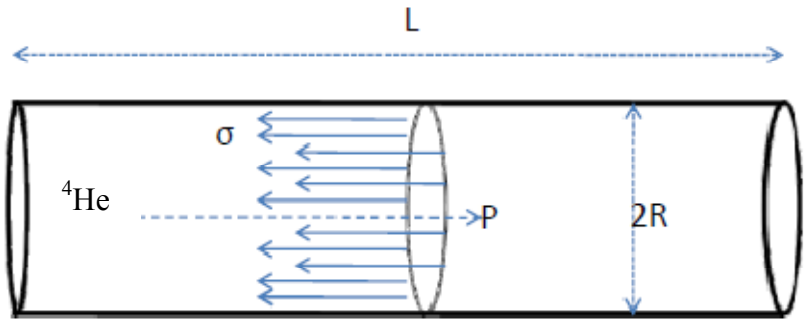

Figure 2.5: Pressure and stress in a cylindrical geometry.

In terms of the pressure gradient along the cylinder

$$\sigma = \Delta P \cdot \frac{R}{2L} = \nabla P \cdot \frac{R}{2} \tag{2.6}$$

since $\nabla P = \Delta P / L$. It is also clear from equation (2.6) that the stress in a crystal depends on the geometry of the cell.

2.7 Pressure measurement and heat capacity of solids

Heat capacity is a thermodynamic quantity, the amount of heat needed to raise the temperature of a substance. According to the Debye model the low temperature specific heat of a solid due to phonons is,

$$C_V = A_{Debye} T^3 \tag{2.7}$$

where A_{Debye}, the coefficient of the cubic term, is a constant which depends only on the properties of the material. In glasses, there is also a linear contribution to heat capacity which we will address in a later section. Insulating materials like solid ^{4}He have very small heat capacities at low temperature, which makes the exact measurement of C_V difficult. This is because a calorimeter (made of metal) has a larger heat capacity than the solid ^{4}He. Many experiments [26, 27, 28] attempted to measure C_V of solid ^{4}He but the calorimeter contribution dominated the measurements. However, a recent experiment [29] used an experimental cell made from silicon. The very small heat capacity of silicon at low temperature makes reliable C_V measurements for solid ^{4}He possible. This experiment found a peak in heat capacity at around 75 mK that might be related to a supersolid phase transition. The low temperature heat capacity has also been analyzed assuming a linear term in the heat capacity [21].

For materials like solid ^{4}He, thermodynamic information can be obtained using a different approach which does not involve calorimeter contributions, by

measuring the temperature dependence of the pressure. This is related to the heat capacity by the Mie-Gruneisen equation, which has the form

$$\left(\frac{\partial P}{\partial T}\right)_V = \sum_i \frac{\gamma_i C_i}{V} \tag{2.8}$$

where, γ_i and C_i are respectively the Gruneisen parameter and heat capacity for the ith subsystem. From this equation the system pressure is

$$P(T) - P_o = \sum_i \frac{\gamma_i}{V} \int C_i dT \tag{2.9}$$

which for phonons gives

$$P(T) - P_o \approx \sum_i \frac{\gamma_i}{V} A_{Debye} T^4 \tag{2.10}$$

The above two equations (2.7 & 2.10) can be simplified to give the average Gruneisen parameter as

$$\gamma \approx \frac{P(T) - P_O}{C_V} \cdot \frac{V}{T} \tag{2.11}$$

In a perfect solid ^{4}He crystal the heat capacity and pressure change are due to phonons. However, in disordered solid ^{4}He, there may also be contributions from two level systems [30] so reliable measurement of γ will become more complicated.

2.8 Linear heat capacity and Two Level Systems

A linear term in the heat capacity of an insulating solid is usually associated with two level systems in glasses and disordered solids. Heat capacity measurements for solid ^{4}He also show signs of a linear [29] term. A corresponding signature, which may be related to two level systems (glass), has also been found in pressure measurements [6, 7].

The Gruneisen relationship (2.8) suggests that a linear temperature dependence in the heat capacity should produce a quadratic temperature dependence in the system pressure. The heat capacity of a Debye solid with disorder is expected to be of the form

$$C_V = B_{TLS}T + A_{Debye}T^3 \tag{2.12}$$

The corresponding pressure is

$$P - P_O = B'_{TLS}T^2 + A'_{Debye}T^4 \tag{2.13}$$

The coefficient of the linear term in heat capacity (B_{TLS}) or the T^2 term in pressure (B'_{TLS}) are the two level system contributions. Rewriting (2.13) as

$$\frac{P - P_O}{T^2} = B'_{TLS} + A'_{Debye}T^2 \tag{2.14}$$

allows one to determine B'_{TLS} by plotting $(P\text{-}P_o)/T^2$ against T^2 (Figure 2.6), giving a straight line. The intercept on the vertical axis gives B'_{TLS} and the slope gives

A'_{Debye}. Previous experiments revealed a T^2 term in pressure for solid ^{4}He with a value of the coefficient (B'_{TLS}) in the range 0.001-0.002 bar-K^{-2} [6, 7]. However, it is not clear whether pressure measurement is equivalent to heat capacity in the case of two level systems.

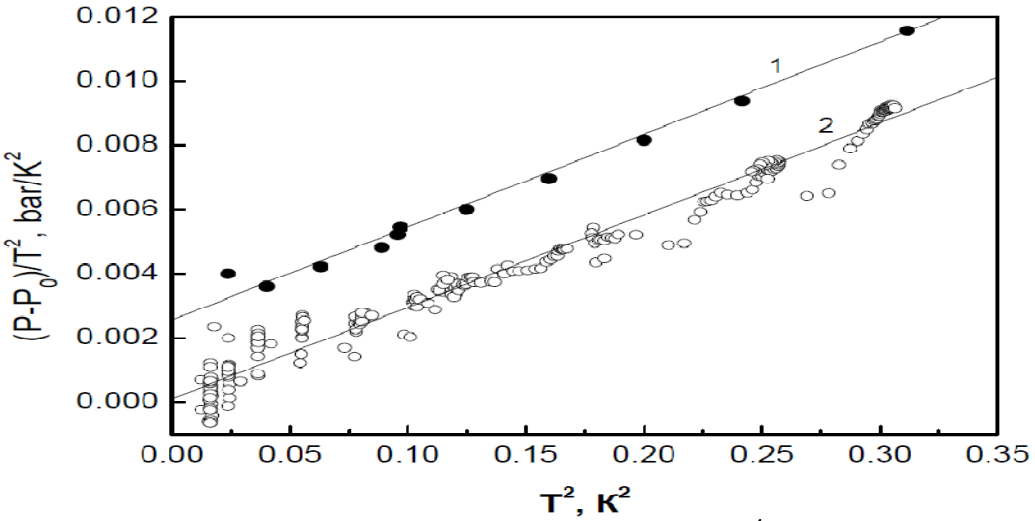

Figure 2.6: Temperature dependence of pressure for solid ^{4}He crystal illustrating the quadratic pressure term. Glassy coefficient of ~0.0025 bar/K^2 is observed in plot 1 (molar volume 20.23 cm^3/mol). Removal of the glassy intercept by means of annealing is shown in plot 2 (molar volume 19.83 cm^3/mol). [6]

As stated earlier, the ratio of pressure to heat capacity is defined as the Mie-Gruneisen parameter. We can define this parameter for two level systems (TLS) and the Debye contribution separately

$$\gamma_{TLS} = \frac{B'_{TLS}}{B_{TLS}} \tag{2.15}$$

$$\gamma_{Debye} = \frac{A'_{Debye}}{A_{Debye}} \tag{2.16}$$

The parameter, γ_{Debye} for solid ^{4}He is well defined; its value ranges from 2.6-3 [31]. The case of γ_{TLS} for solid ^{4}He is much less clear. It has been studied in the case of other disordered solids [32]. However its value varies over a wide range and it depends strongly on temperature. Since the Gruneisen relation for TLS is not well established, it is not clear that pressure measurements give the same thermodynamic information as heat capacity.

2.9 Thermally activated defects

Defects are important in determining the properties of solid ^{4}He. Most of the unusual behavior observed in solid ^{4}He is linked to the presence of defects and they play a key role in the supersolid phase of ^{4}He. The presence of defects in solid ^{4}He crystal is highly temperature dependent. There are some non-thermal defects like dislocations that remain at low temperature but others like vacancies are thermally activated and disappear at low temperature. Wavefunctions overlapping between neighboring lattice sites in a quantum crystal enable movement of vacancies even at zero temperature and an increase in temperature allows additional thermal hopping. This movement of vacancies can help relax stresses in crystals [33]. Such stress relaxation can be observed in pressure measurements during an annealing process. Low temperature relaxation of pressure [7] has been observed during annealing of a disordered crystal.

Our experimental plan is to produce highly disordered crystals and also to eliminate this disorder by annealing. Thermally activated relaxation of defects can

be studied during this process from the temperature and time dependences since the time required for obtaining thermal equilibrium takes different values at different temperatures. By measuring this rate at different temperatures, we hope to determine the activation energy of the defects.

The Arrhenius equation relates the rate of a thermally activated process to the activation energy and temperature. The relation has the form

$$\kappa = \frac{1}{\tau} = Ae^{-\frac{E}{T}} \tag{2.17}$$

where κ, τ, E and T are the rates of the thermal process, the time constant, the activation energy and the temperature respectively. 'A' is referred to as the attempt frequency of the process. To calculate the activation energy, this equation can be rewritten as

$$\ln\left(\frac{1}{\tau}\right) = \ln A - \frac{E}{T} \tag{2.18}$$

If the logarithm of the rate is plotted against the inverse of T then the slope of the curve will give the activation energy (E) of this thermal process. An activation energy for a 42.5 bar crystal has been calculated in this way for the low temperature pressure relaxation in previous experiments [7], as shown in Figure 2.7. The time constant (τ) of the thermal relaxation process was determined at each temperature. Then the logarithm of this time constant was plotted against inverse of that temperature to generate the expected straight line whose slope

gives the activation energy, as shown in Figure 2.7. An activation energy of 28 mK describes this low temperature pressure relaxation.

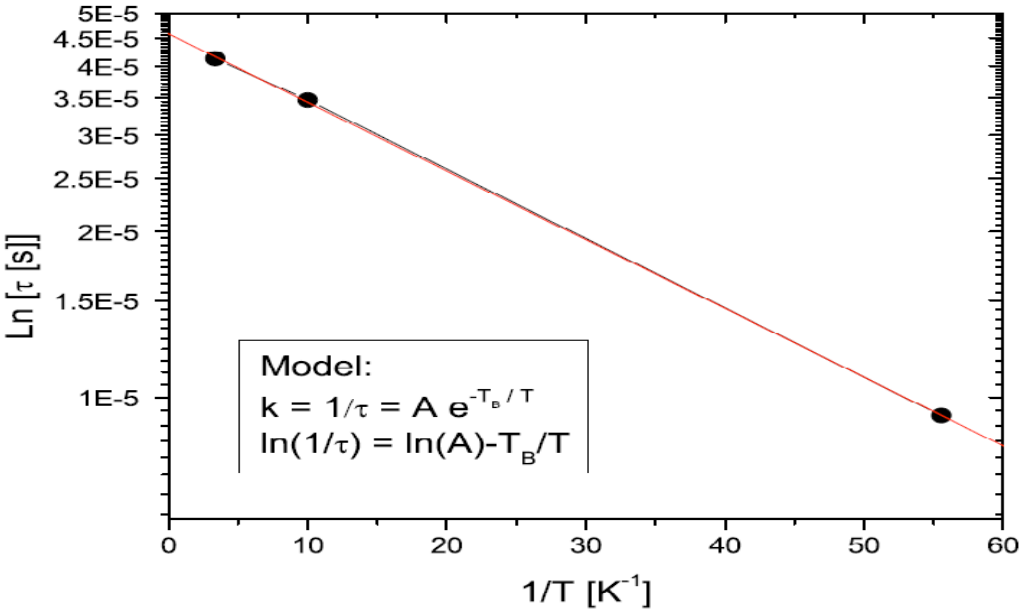

Figure 2.7: Logarithm of thermal time constants at three different temperatures 19, 100 and 300 mK are plotted against inverse temperature in the case of low temperature pressure relaxation of a 42.5 bar crystal. The symbols K, τ, A and T_B (=E) refer to rate, response time, attempt frequency and activation energy of any thermal process. Slope of this curve gives the activation energy (T_B = E) of the process. A value of 28 mk has been found. Taken from [7].

Thus thermal relaxation of pressure in a crystal can be utilized to give access to the calculation of activation energy of the relaxation process in that crystal.

2.10 Goals of the thesis

Supersolid properties of solid ^{4}He have been described in this chapter along with their dependence on defects. Detailed discussions have been provided about the relationship between the following properties: 1) stress, plastic flow & defects, 2)

pressure gradient & stress, 3) temperature dependence of pressure & heat capacity and 4) annealing & thermally activated pressure relaxation processes. The goal of this thesis is to learn about the role and nature of defects in the behavior of solid ^{4}He at low temperature by creating defects and then removing them by annealing. We will use pressure measurements to do this.

The study of defects requires a highly disordered crystal, so we grew solid ^{4}He crystals using the blocked capillary method which favors creation of defects. After growth, large stresses were produced by means of heat pulsing (rapid heating and partial melting) and quench cooling. Quench cooling was as fast as possible to introduce and retain the maximum number of defects. Pressure differences allowed the measurement of yield stresses in the disordered crystal, using the geometry of the cell. The temperature dependence of pressure was measured to investigate possible glassy states (two level systems) in solid ^{4}He. Following that, the disordered crystal was annealed and the time and temperature dependence of pressure relaxation in solid ^{4}He will be discussed. The pressure relaxation at low temperature was studied to see whether the annealing process is thermally activated and to identify the annealing mechanism.

Chapter 3

Experiment

As discussed in the previous chapter, the objectives of the experiments are to study solid ^{4}He crystals in the presence and absence of defects. Heat pulses and thermal quenching are effective ways to create defects. Pressure measurements give information about pressure gradients as well as about relaxation processes and possible glassy contributions to thermodynamic properties. Accurate measurements of pressure and temperature require great deal of attention to be paid to the experimental design. The following chapter will discuss the design of the experiment with explanation of the factors that influence such designs as well as with techniques of measurements.

3.1 Cell geometry and construction

The experimental cell (Figure 3.1) is of cylindrical shape with a cylindrical space inside it for solid ^{4}He. The cell is made of oxygen free high conductivity copper. It has two pressure gauges attached on the opposite ends. There are spaces on the cell's outer surface for connecting several thermometers and heaters. The dimensions of the cell are as follows:

Outer length of the cell = 5.1 cm

(a)

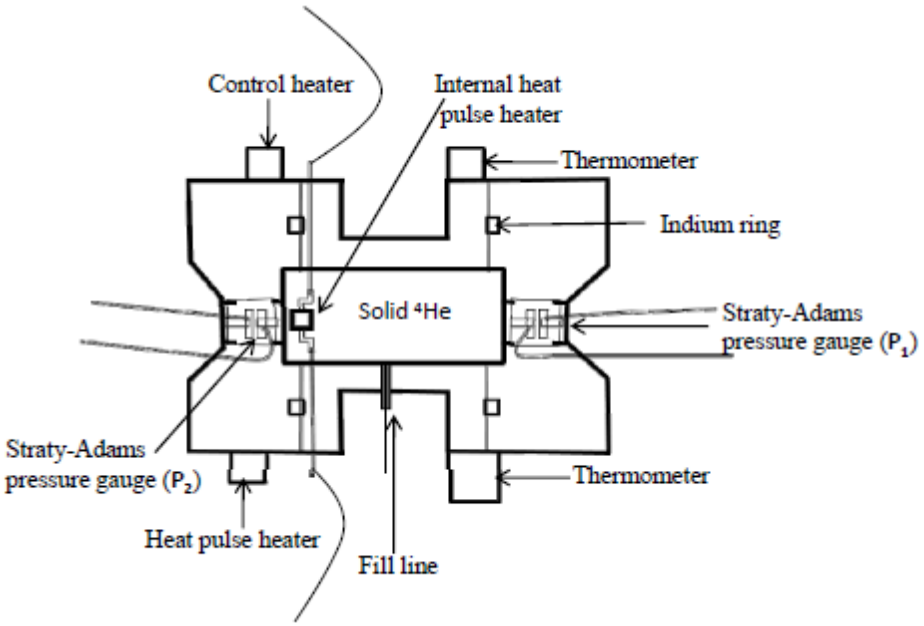

(b)

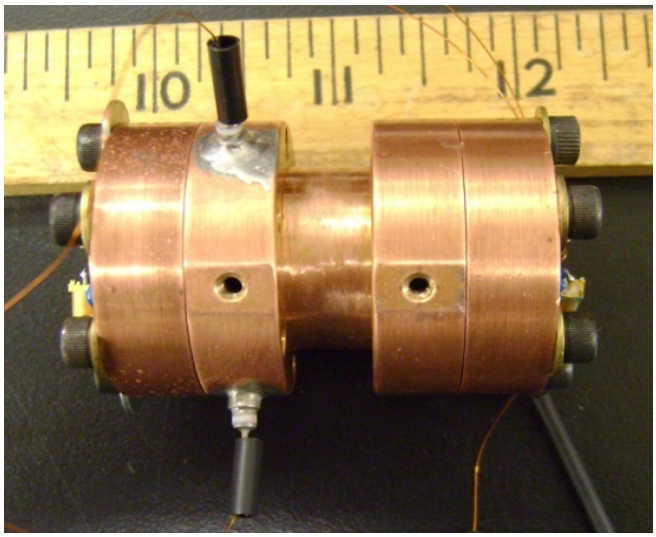

Figure 3.1: (a) Schematics of the experimental cell with all important parts indicated. The cell is made of OFHC copper. Two S.A pressure gauges are connected at the opposite ends of the cell. As usual there are heaters and thermometers connected to the cell. All the three heaters are shown including the internal one. There are two indium O-rings sealing the cell. Ceramic feedthroughs (CeramTec, Part #9297-03-W) are used on the cell to connect the internal heater to the outside coaxial cables. (b) a real picture of the cell.

Outer radius of the cell =1.9 cm

Length of the solid ^{4}He space (h) = 3.05 cm

Radius of the solid ^{4}He space (r) = 0.76 cm

Therefore, the volume of solid ^{4}He inside our cell will be,

$$\text{Volume} = \pi r^2 h = 5.56\ cm^3$$

One of the unique features of the cell is its two pressure gauges positioned at opposite ends. A single pressure gauge only provides information about pressure at a point in a crystal. To know whether there is a gradient (∇P) in the crystal or whether the average pressure goes up or down in any thermodynamic process, another gauge is needed. Using the two pressure gauges, we can measure a pressure difference ΔP and get an idea of ∇P and the resultant stress σ. Moreover, we can get some sense of whether either of the gauges is measuring the true equilibrium pressure P(T).

Three thermometers and two heaters are used for thermodynamic measurements. The heaters have resistances of 200 ohm and 1000 ohm. The 200 ohm heater is used for temperature control whereas the 1000 ohm heater is a specialized one used for applying heat pulses. The cell is constructed in such a way that the heat pulse heater (CADDOCK, Model #MP 820) can be placed inside the cell, embedded within the solid ^{4}He; alternatively a similar heater can be mounted outside the cell on the OFHC copper surface. The heat pulse heater (internal) is square shaped with a surface area of 32 mm^2 on both sides. The

external heat pulse heater is also of square shape but with a higher surface area 170 mm^2. Two ceramic feedthroughs are inserted into the cell for connecting the internal heater. The cell, along with the thermometers and heaters is attached to the mixing chamber (MC) of the dilution refrigerator (Figure 3.2) where the experiment is being performed.

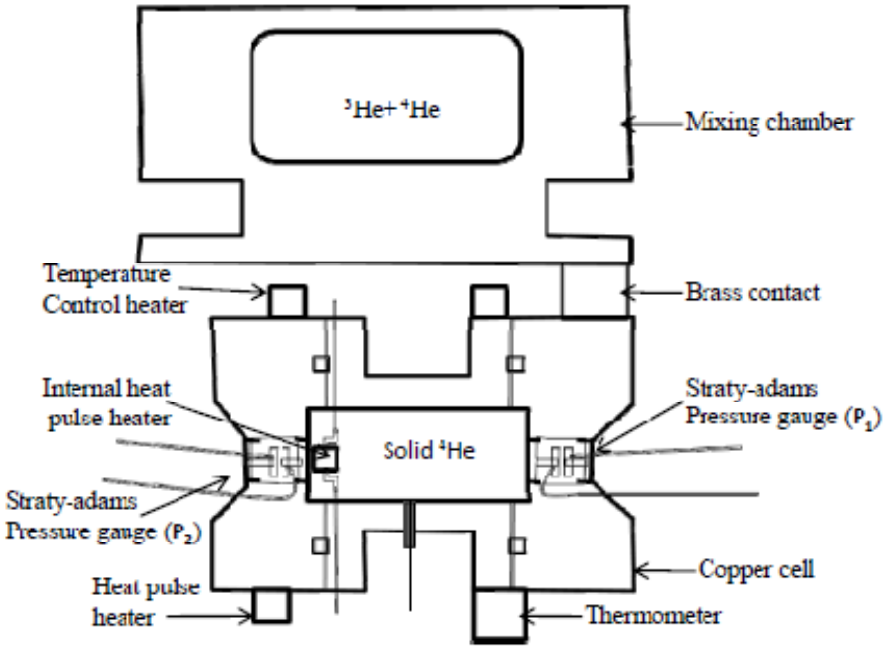

Figure 3.2: Schematic of the cell mounted on the mixing chamber of the fridge. P_1 and P_2 are the two Straty-Adams pressure gauges. $((P_1+P_2)/2)$ gives the average pressure.

3.2 Cooling Technique, Thermometers and Pressure Gauges

3.2.1 Dilution Refrigerator

We used our dilution refrigerator (SHE DRP-42) for cooling our samples. It has a base temperature of 11 mK without any external heat load. Recently we have tested it to be 16 mK with our sample cell connected to the mixing chamber. The cooling power of the refrigerator is 300 μW at 100 mK temperature. The main cooling part of the fridge is the mixing chamber that holds the ^{3}He and ^{4}He mixture. The volumes of ^{3}He and ^{4}He in the mixing chamber are 5.8 cm^3 and 8.8 cm^3 respectively. The experimental cell is connected with the mixing chamber to do the experiment.

3.2.2 Temperature Measurement

The experiment will be done at very low temperature. Therefore reliable thermometry has to be used. One of the major problems of low temperature thermometry is long thermal response times. Therefore, a thermometer has to be chosen such that its thermal response time is small. There are three different types of thermometers used in our dilution refrigerator. They are: 1) Germanium Resistance Thermometer, 2) ^{3}He Melting Curve (MC) thermometer and 3) ^{60}Co Nuclear Orientation (NO) Thermometer.

^{3}He MC and ^{60}Co NO thermometers are primarily used for measurements below 50 mK. Our temperature range of interest in the proposed experiment is above 50 mK. The germanium (Ge) thermometer (Figure 3.3) is very reliable for

measuring temperature above 50 mK. In this temperature range the Ge thermometer is highly sensitive, responds quickly and shows reliable stability in

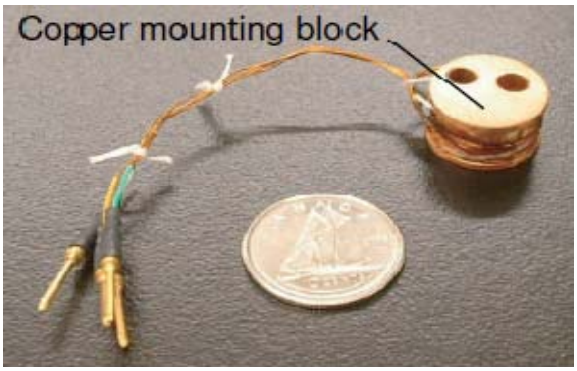

Figure 3.3: Germanium thermometer mounted on copper block. Dime is used for scale.

calibration. The Germanium thermometer was used for all temperature measurements in this experiment. At 4.2 K it has excellent stability of ± 0.5 mK and 200 ms thermal response time [34]. The thermometers are connected to a very reliable digital resistance bridge (Conductus LTC-21 or Neocera LTC-21) for measuring and controlling the temperature.

3.2.3 Pressure Measurement

The experimental goal is to analyze pressure measurements made on solid ^{4}He crystals for studying the behavior of highly stressed crystals. This makes pressure the most important parameter in this experiment. All the pressure measurements are made by homemade Straty-Adams [35] pressure gauges (Figure 3.4) that are reliable for low temperature measurements. The advantage of this pressure gauge is its ability to measure pressure in situ. The in situ pressure measurement is very

important in the case of a solid. During blocked capillary crystal growth (discussed in section 3.3.1), the solid plug in the capillary at low temperature makes pressure measurements impossible with conventional room temperature pressure gauges. This is due to the difference in pressure between the low temperature sample cell and the rest of the experimental system.

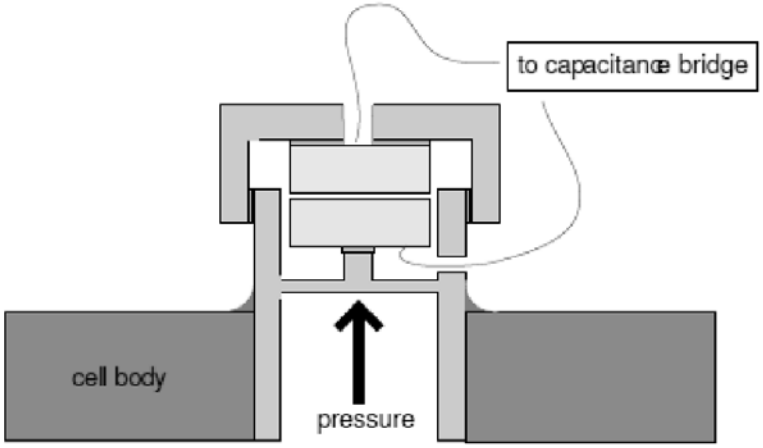

Figure 3.4: Schematic of a Straty-Adams pressure gauge attached to the cell.

Our Straty-Adams pressure gauge uses a capacitive technique to measure pressure. Its body is made of hardened BeCu with a diaphragm of 0.2 mm thickness machined at the middle. This part is attached to the region whose pressure is to be measured. The diaphragm flexes in response to any change in pressure of the sample but it does not respond to shear stress. There are two small circular brass plates, one attached on a small post on the diaphragm and the other one attached to the brass cap. These two plates act as a parallel plate capacitor. Any change in pressure in the sample produces a change in the capacitance of the pressure gauge. This change in capacitance is converted to pressure using a calibration of the pressure gauge with liquid ^{4}He at high temperature (4.2 K).

Some of the advantages of Straty-Adams pressure gauges are high sensitivity, extreme stability at low temperature, absence of hysteresis, very small self-heating and little influence of temperature below 4.2 K.

The capacitance of the pressure gauges is measured using an Andeen-Hagerling 2550A capacitance bridge, an automatic digital bridge operating at a frequency of 1 kHz. The bridge is connected to each pressure gauge via two coaxial cables in a "three wire" configuration. The sensitivity of our pressure gauges when measured by the capacitance bridge is 50 μbar. This is equivalent to a capacitance sensitivity of 10^{-5} pF. The resolution of our digital bridge is 10^{-7} pF.

3.2.4 Heater selection

There are two different heaters used in our experiment: 200 ohm and 1000 ohm. The 200 ohm heater is used for controlling temperature of the fridge and the sample cell. It is connected with one of the temperature controllers, along with the Ge thermometer, to control the temperature of the system. The 1000 ohm heater is the one used for applying heat pulses to the sample cell to deform the crystal. For heat pulses, either a 200 or 1000 ohm heater can be used but the smaller the resistance of the heater, the higher will be the power dissipated in the leads connecting the heater and the power supply. This power dissipation reduces the cooling power of the fridge. Thus a higher resistance heater is used for heat pulsing to let the fridge cool without experiencing any significant extra heat load. This of course requires higher voltage to be applied. Coaxial cables and thermally

anchored wires are used for connecting the heater with the output power supply to reduce any additional heat load.

3.3 Crystal growth method and creating defects in crystal

3.3.1 Growth Method

Even at low temperatures, growing solid ^{4}He crystals requires the application of 25 bar or more pressure. Different techniques can be used for growing ^{4}He crystals. They are constant pressure, constant temperature (from the superfluid region of ^{4}He) and constant volume (Blocked Capillary) method. The first two methods are used for growing crystals with higher crystalline order [36, 37]. There is a consensus that crystals grown using the blocked capillary method are of lower quality [37] than with the other two methods. We used the blocked capillary method since our intention is to have a deformed lower quality crystal. All the crystals in our experiment were grown using the blocked capillary method. The blocked capillary method can be explained as follows. In this method the average density remains constant after the blocking, so the growth process must start with liquid at the desired (solid) density. Initially, the cell is pressurized at 4.2 K with the desired liquid helium pressure. This initial pressure value is determined from the phase diagram (Figure 3.5) using the pressure value at which

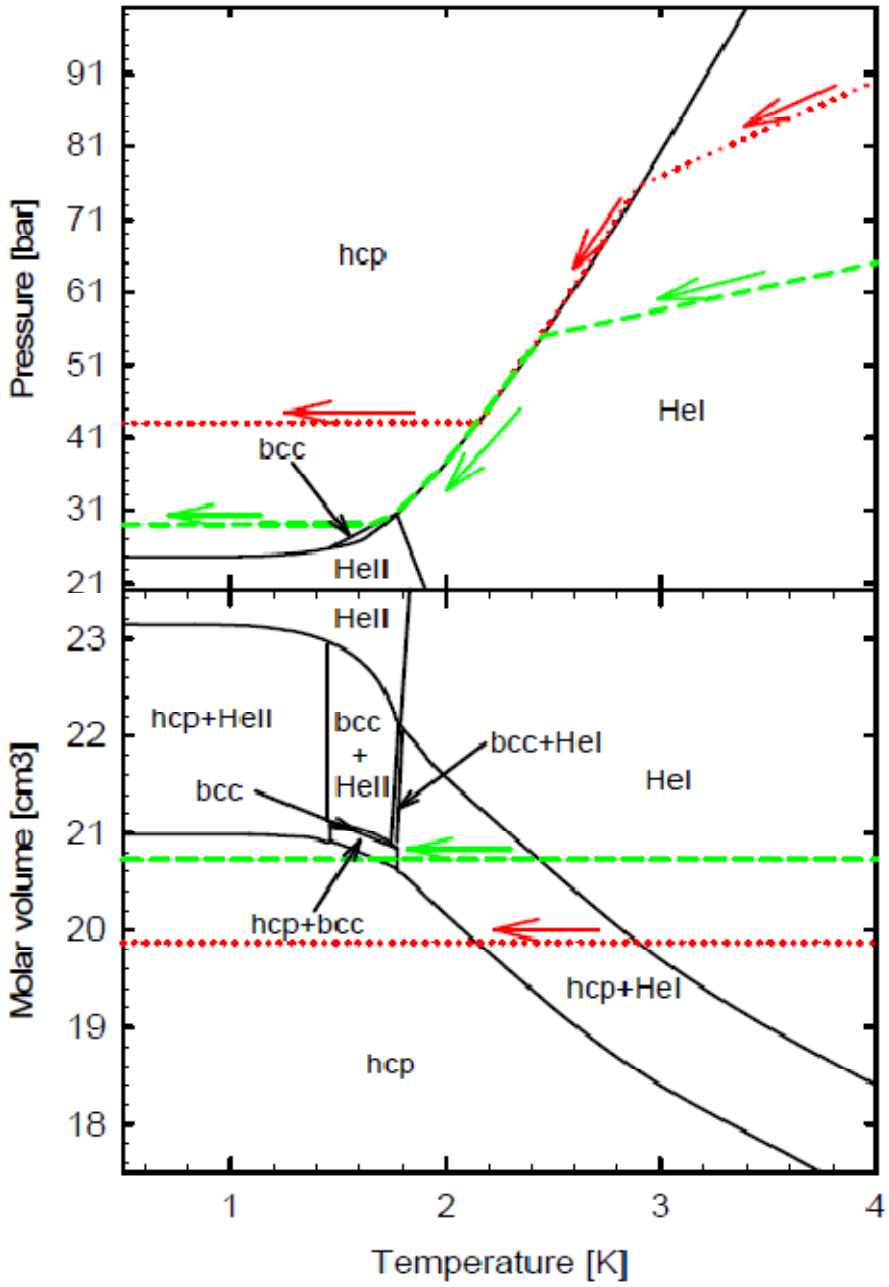

Figure 3.5: Phase diagram of solid ^{4}He. It guides in finding the pressure and molar volume of a crystal grown at certain temperature. Thermodynamic paths for growth of two blocked capillary crystals (43 bar and 28 bar) are shown.

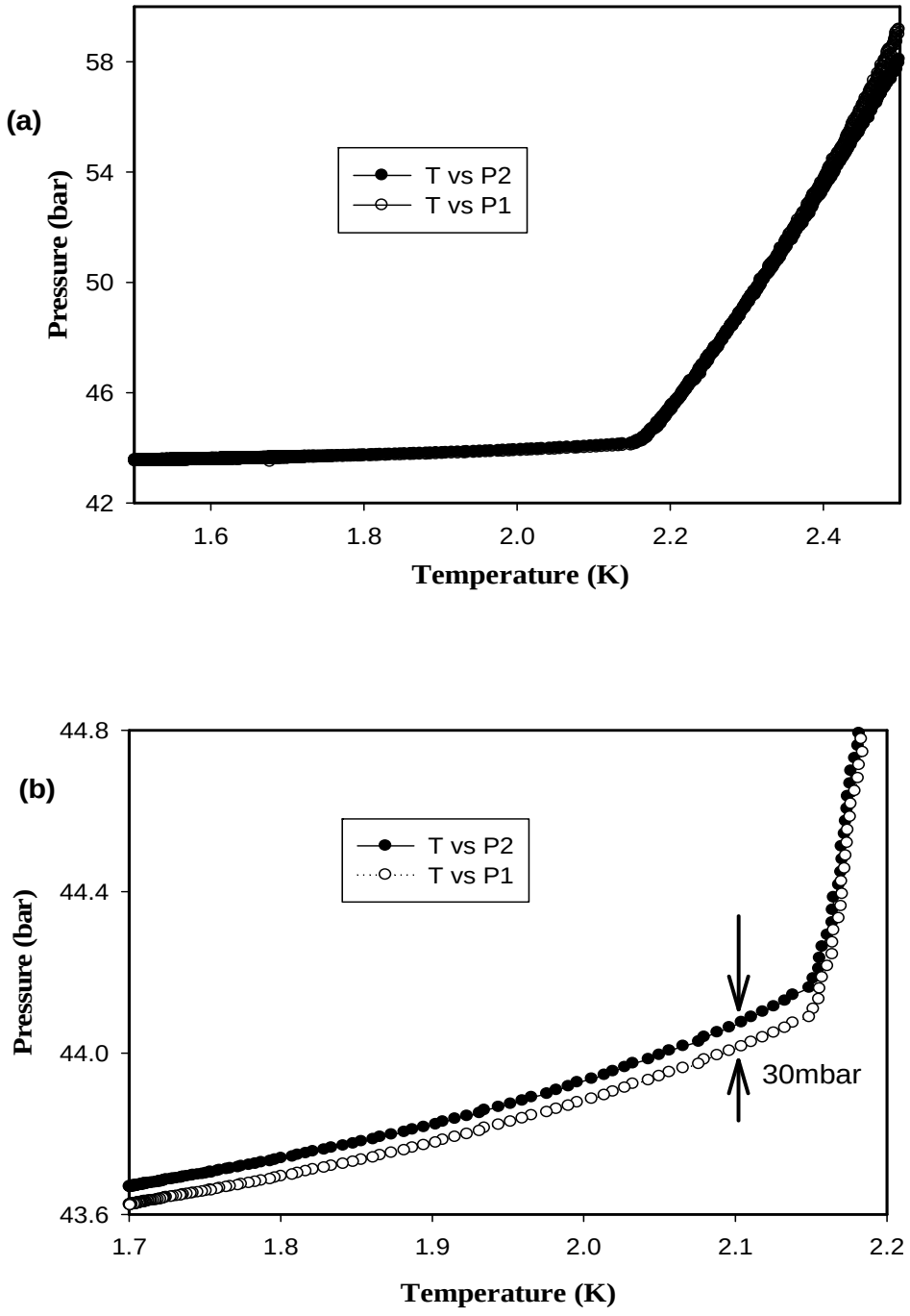

Figure 3.6: Pressure versus temperature plot for the two S.A. gauges during the final stage of the growth of a solid ^{4}He crystal. (a) the identical behavior of both pressures (closed and empty circles) as it follows the melting curve and (b) a blown up region of (a) with indication of 30 mbar pressure gradient after freezing is complete.

we want the crystal to be formed. The capillary used for filling the cell is anchored at different places on the fridge such as the 1 K pot, still, heat exchanger etc. If, after pressurizing, cooling is started by pumping on the 1K pot, then the 1 K pot of the fridge will cool within couple of minutes, blocking the capillary with solid ^{4}He from the outside gas handling system (GHS). Now as the fridge continues to cool, the volume of the ^{4}He inside the cell will remain constant but the pressure will drop with temperature. Then this constant volume ^{4}He will start solidifying at certain temperature, following the melting curve until all liquid is frozen, at which point it will leave the melting curve. Further cooling of the crystal formed by this method occurs at constant volume too. Figure 3.5 shows the phase diagram with the thermodynamic paths for two crystals. On the phase diagram the dotted line is for a 43 bar crystal whereas the short dashed one is for a lower pressure crystal which passes through the bcc/hcp phase. The experimental data for growing one such constant density crystal is shown in Figure 3.6.

Two pressure gauges in our cell allow us to see the pressure in the crystal in more detail. Figure 3.6 shows the temperature versus pressure plots made for the two different gauges of the cell for a 43.5 bar crystal. In Figure 3.6, (a) shows the crystal following the melting curve and both pressures look to be identical. But if (a) is blown up in a small temperature region, as shown in (b), then it becomes clear that there is a pressure gradient between the two ends of the crystal. The value of the pressure difference is found to be around 25-30 mbar. This gradient originates from the stresses produced in the crystal due to the large pressure drop

as a result of blocking the capillary. This pressure gradient creates a crystal with defects (as discussed in chapter 2).

3.3.2 Creating more defects in the crystal

The blocked capillary method produces crystals with defects. Further defects can be created by means of a heat pulse followed by quench cooling. By "heat pulses" we mean rapid changes in temperature of the crystal. And "quench cooling" refers to the cooling of the crystal as rapidly as possible following a heat pulse. Heat pulses introduce a sudden temperature change and a temperature gradient in the crystal. This temperature gradient produces a pressure gradient through thermal expansion of the solid or through partial melting of the crystal. The pressure gradients can cause plastic deformation, which creates defects like dislocations. If a heat pulsed crystal is quench cooled to low temperature, annealing is minimized and pressure gradients and defects will remain at low temperatures.

Figure 3.7 shows an example of such a heat pulse (internal heater) where the crystal is heated from the base temperature to above its melting point in five seconds, followed by quench cooling to 0.4 K in less than half a minute. Heat pulses can create 250 mbar of pressure difference between the gauges compared to the 30 mbar pressure difference which existed in the crystal before the heat pulse. Significant stress is introduced into the crystal by these large gradients. This gradient is due to, rise in crystal's pressure at one end and lowering at the other. The presence of the heat pulse heater at the P_2 end results in pressure increase at P_1 and pressure decrease at P_2 during quench cooling.

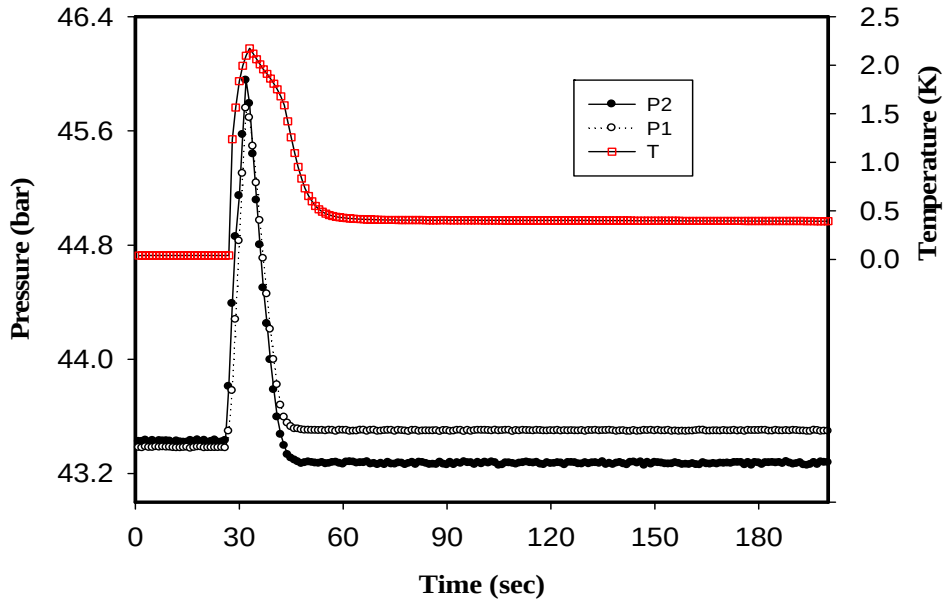

Figure 3.7: Pressure and temperature curve in response to a heat pulse (internal heater). Note the increase in the pressure gradient in the crystal due to the pulse.

Heat pulses should not be applied for longer than necessary to melt part of the crystal. Otherwise, the additional heat will warm up the fridge's mixing chamber. One of our goals is to quench cool the sample using the heat capacity of the mixing chamber. Additional heating warms the mixing chamber which then cools much more slowly because of the fridge's limited cooling power. This makes the thermal time constant for thermal equilibrium between the cell and the mixing chamber an important parameter in this experiment.

3.4 Thermal Time Constants

The mixing chamber of a dilution refrigerator is made of copper and it contains a mixture of ^{3}He and ^{4}He in an internal cylindrical space. The experimental cell is made of oxygen free high conductivity copper. It holds solid ^{4}He inside a

cylindrical space. The design of the cell is such that heat can be applied directly to the outer surface or otherwise straight to the solid ^{4}He internally by a heater embedded in the ^{4}He.

An important part of our experiment is to apply heat pulses to the sample cell, followed by quench cooling. A cell is normally connected directly to the mixing chamber. In this case, most of the heat applied to the sample cell will go to the mixing chamber, warming it up. This interrupts the fridge's cooling power and prevents us from quench cooling. Therefore, some sort of thermal weak link has to be placed between the cell and mixing chamber. This weak link (thermal contact) can be made of Cu, brass or stainless steel. It will be used to control the time constant between the cell and mixing chamber. There are also thermometers and heaters connected to the sample cell whose response times are also important. A schematic of the cell connected with the mixing chamber is shown in Figure 3.8. As this figure shows, a heat pulse applied to the Cu cell will flow from the cell to the solid ^{4}He, and they will come in thermal equilibrium with a time constant $\tau_{cell+Helium}$. At the same time some heat will flow to the mixing chamber with a time constant $\tau_{cell+mixing\ chamber}$. If a heat pulse is applied directly to the solid ^{4}He then it will similarly warm up the cell and thermometers and achieve equilibrium with some of the heat travelled to the mixing chamber. In both cases

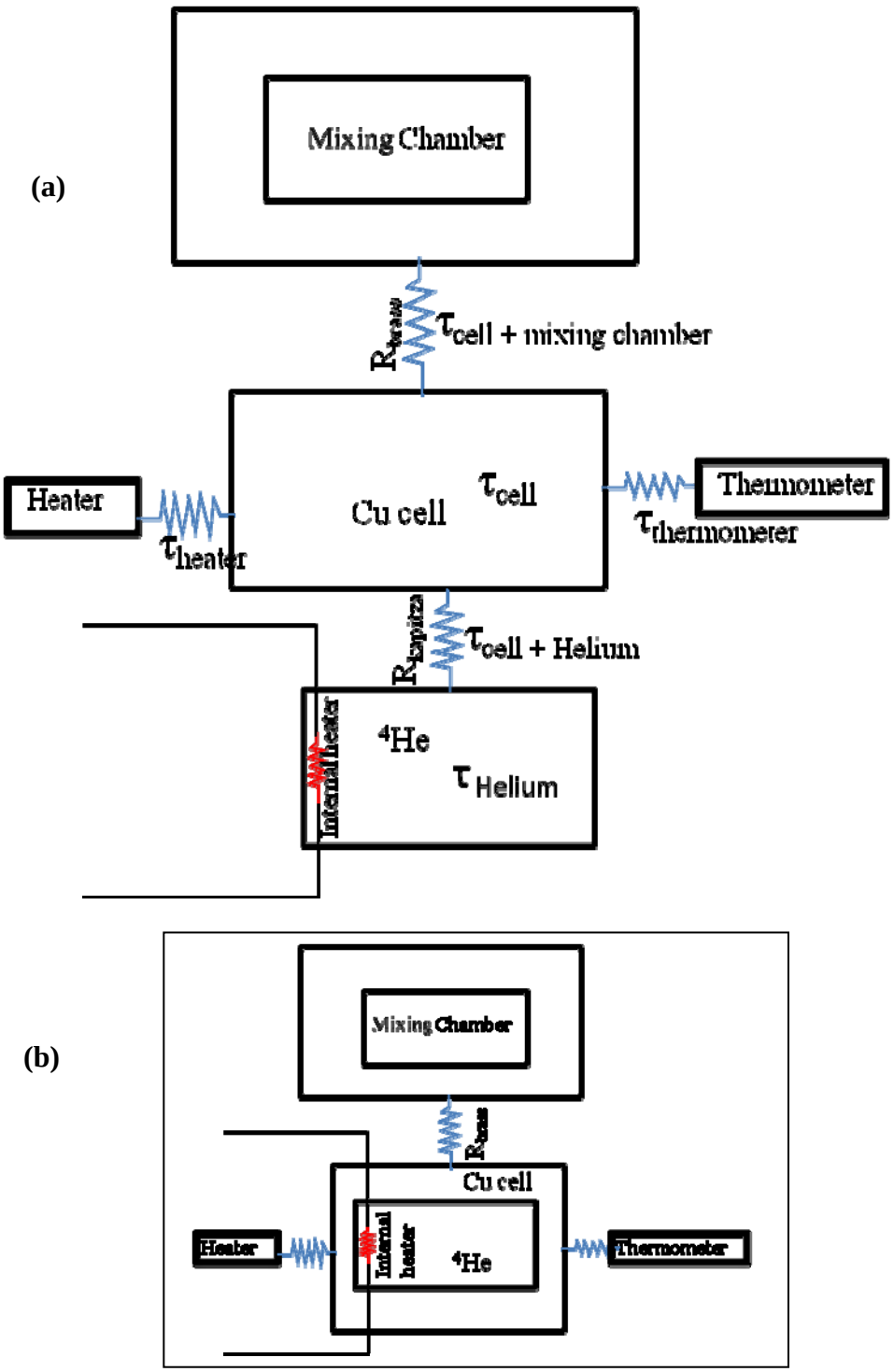

Figure 3.8: (a) Heat flow between solid ^{4}He, cell, mixing chamber and thermometers. Different materials have different time constant depending on the material properties. (b) the arrangement with solid ^{4}He inside the Cu cell. In the figure τ's are the thermal response time, R_{brass} is the brass thermal resistance and $R_{Kapitza}$ is Cu-solid ^{4}He boundary resistance.

thermal time constants are involved in each step of flow. The thermal time constants between parts of the system, such as solid ^{4}He to Cu cell($\tau_{\text{cell + Helium}}$) or vice versa, Cu cell to thermometer($\tau_{\text{cell + thermometer}}$), Cu cell to mixing chamber ($\tau_{\text{cell + mixing chamber}}$), and the internal time constants for ^{4}He(τ_{Helium}) and Cu cell (τ_{cell}) determine the response to heat pulses.

The variations in time constant arise from the thermal properties of the materials. Also, between solid ^{4}He and the Cu cell there exists a boundary resistance at the contact surface, known as the Kapitza resistance. This boundary impedance controls the thermal time constant between solid ^{4}He and the Cu cell. It is expressed by the empirical relation, $R_{kapitza}=0.002/AT^3$ (m^2K^4/W) [38]. This Kapitza resistance was determined for the case of a 31 bar crystal. Here 'A' is the contact surface area between solid ^{4}He and copper. Design of an experiment that involves application of large efficient heat pulses and quench cooling, requires knowledge of all thermal time constants.

In general the thermal time constant is the time required for a system's temperature to approach equilibrium. This could be the time needed for heat flow from one part of the system to another part connected by a thermal contact or it might be the internal time for heat to transfer from one point to another within a single part. A thermal response time can be defined by the formula,

$$\tau = R \frac{C_1 C_2}{C_1 + C_2} \tag{3.1}$$

where, τ and R are the thermal response time of the system and thermal resistance of the thermal contact and C_1 and C_2 are the heat capacities of the two parts of the system involved in the response time constant measurement. The thermal resistance R depends on the thermal conductivity and the dimensions of the thermal contact. It is given by the formula,

$$R = \frac{1}{\kappa} \frac{L}{A} \tag{3.2}$$

where κ, L and A are respectively thermal conductivity, length and cross sectional area of the contact. Thus the thermal response time between two different materials can be calculated using equation (3.1) and (3.2) if the heat capacity of the two materials and thermal conductivity and dimensions of the contact between them are known.

However, this is different in the case of internal heat transfer in a material. Then, the heat capacity $C_1 \approx C_2 \approx C/2$, where C is the total heat capacity of this material and the thermal response time in equation (3.1) can be written as,

$$\tau = R \frac{C}{4} \tag{3.3}$$

The thermal time constant for a material is calculated by substituting the thermal resistance formula from equation (3.2) and using the heat capacity per unit volume of this material. Then equation (3.3) will take the form,

$$\tau = \frac{1}{\kappa}\frac{L}{A}\frac{c.(L.A)}{4}$$
$$\tau = \frac{c}{\kappa}\cdot\frac{L^2}{4} \qquad (3.4)$$

so the internal thermal time constant of any material can also be calculated using the values of heat capacity, thermal conductivity and length of the material. For the present experiment, these thermodynamic values can be calculated using expressions in tables 3.1-3.4.

3.5 Calculating thermal time constants

So far we have learned that the thermal response time depends on thermodynamic properties like heat capacity and thermal conductivity and also on the sample cell's geometry. In our experiment the materials involved are solid ^{4}He, liquid ^{4}He and ^{3}He, Cu and brass. At low temperature, the behavior of copper and brass is straight forward, as shown in the Table 3.1, since they are metals.

However the properties of solid ^{4}He, liquid ^{4}He and liquid ^{3}He have discontinuous temperature dependences. Their thermodynamic behavior cannot be expressed by a simple formula like in the case of brass and copper. They exhibit

different temperature dependence in different ranges of temperature. To calculate thermal time constant the temperature range of interest has to be decided at the beginning. In our experiments, temperature of solid ^{4}He varies from 50 mK to 2.2 K, but time constant are only important in the range 1-2 K, as this is the region where most of the quench cooling of the sample is done. However, the response time at low temperature is also worth knowing. Also, there is liquid ^{3}He and ^{4}He inside the mixing chamber and their temperature never exceeds 0.5 K during the experiment. The temperature range of operation for different parts of the experiment is given in Table 3.2.

Name of Metal	**Copper (Cu)**	**Brass**
Heat Capacity	$C_V = 0.00063T + 0.00017T^3 [J/mole.K]$	----
Thermal Conductivity	$\kappa = 1366T \ [W/K.m]$	$\kappa = 0.68T$ $[W/K.m]$

Table 3.1: Thermodynamic property of copper and brass at low temperature [39].

For the ^{4}He and ^{3}He no formula is available for the whole temperature range but from around 100 mK to 500 mK their temperature dependences can be approximately expressed by empirical formulas shown in Table 3.3.

Experimental materials	Temperature range
Solid ^{4}He	50 mK – 2.2 K
Liquid ^{4}He (MC)	50 mK – 400 mK
Liquid ^{3}He (MC)	50 mK – 400 mK
Cu cell	50 mK – 2.2 K
Brass Contact	50 mK – 2.2 K

Table 3.2: Operational temperature range of each material involved in our experiment.

Property	Solid ^{4}He	Liquid ^{4}He	Liquid ^{3}He
Heat capacity	$C_V = 0.0013T + 0.093T^3$ $[J/mole.K]$	$C_V = 0.035T^3$ $[J/mole.K]$	$C_V = 15T$ $[J/mole.K]$
Thermal conductivity	$\kappa = 41T^{2.3} [W/K.m]$	----	----

Table 3.3: Empirical formulas for thermodynamic behavior of ^{4}He (solid & liquid) and ^{3}He (liquid) in the temperature range 100-500 mK [39].

Using formulas shown in the tables, the thermal response time for heat flow within solid ^{4}He, within the Cu cell and between the Cu cell and the solid ^{4}He (and vice versa) can be determined in the temperature range 50-500 mK. One example of such response time calculation regarding heat flow is shown below in the case of solid ^{4}He.

For internal heat flow the response time is calculated using the equation 3.4. This has the form,

$$\tau = \frac{c}{\kappa} \times \frac{L^2}{4}$$

We can calculate the response time at 0.5K by using the value of heat capacity, thermal conductivity from table 3.3 and the length of the material.

The heat capacity of solid ^{4}He is $C = 0.0013T+0.093T^3$ J/mol-K
$= 62T + 4429T^3$ J/m^{3}K

The thermal conductivity of solid ^{4}He is $\kappa = 41T^{2.3}$ W/K.m

Using the heat capacity per unit volume of a solid ^{4}He sample and its thermal conductivity, the thermal response time can be calculated at any temperature. The thermal response time for a 5 cm long solid ^{4}He sample at 0.5 K is,

$$\tau = \frac{1}{41 \times 0.5^{2.3}} \times \frac{(62 \times 0.5 + 4429 \times 0.5^3) \times (0.05)^2}{4}$$

$$\tau = 44\ m \text{ sec}$$

Similarly, we can calculate the thermal response time at other temperatures, as well as for other materials. Plots of thermal time constants have been made in Figure 3.9 in the case of internal heat flow in solid ^{4}He, in Cu and also between solid ^{4}He and Cu.

The internal response times for heat flow within solid ^{4}He, within Cu and also between solid ^{4}He and Cu cell are all less than 100 milliseconds (Figure 3.9). This tells us that if some heat is applied to the cell or to solid ^{4}He then they will come to mutual equilibrium in a fraction of a second. Now if the cell is directly connected to the mixing chamber or if there is a good thermal contact (e.g. Cu) used in between, then much of the heat will be carried to the mixing chamber during a heat pulse of a few seconds. A thermal contact other than Cu has to be used to restrict this heat flow. In this case brass looks to be a good choice due to its smaller thermal conductivity. If we use brass as the thermal contact between the cell and mixing chamber then the response time can be on the order of seconds, as shown in Figure 3.10. This figure shows the response time for the two brass thermal contacts of different dimensions ((1 cm × 1 cm × 1 cm) & (0.5 mm × 6 mm × 9.5 mm))

The response time obtained is significantly higher in the case of brass than in copper. This thermal time can be increased further by a reasonable amount simply by changing dimension of the contact in such a way that the resultant conductivity is decreased. The plots made so far regarding response time are only applicable in the temperature range 50-500 mK.

As mentioned earlier, the important region of temperature is above 1 K. For simplicity, we can calculate the response time numerically in the temperature range above 1 K, using experimental values of C and κ and assuming the heat transfer between the cell and the mixing chamber is equivalent to transfer between

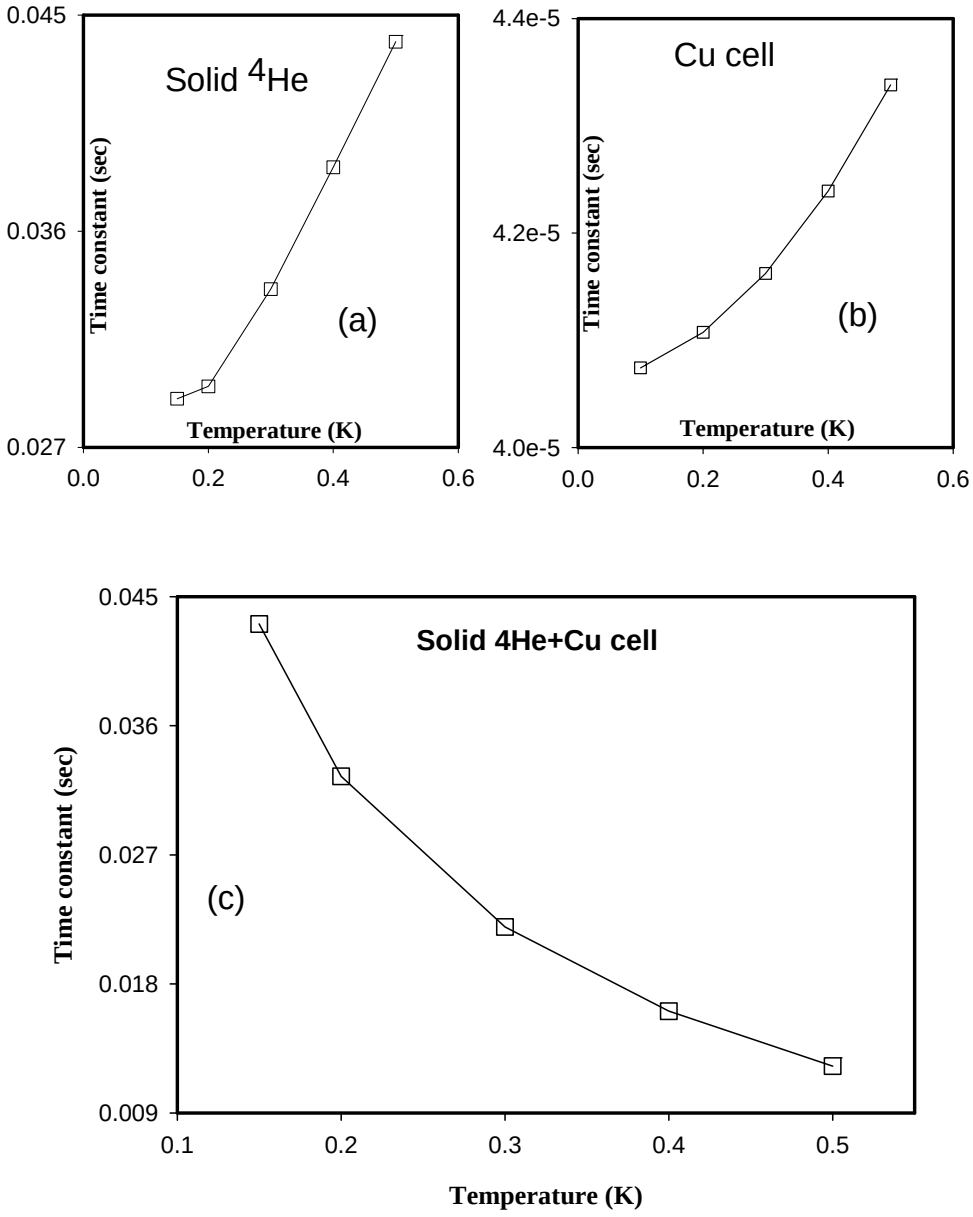

Figure 3.9: Response time for solid ^{4}He and Cu cell in the 100-500 mK temperature range. (a) τ for solid ^{4}He only, (b) for copper only and (c) τ for heat flow between solid ^{4}He and copper cell. Notice, the small response time in all the cases.

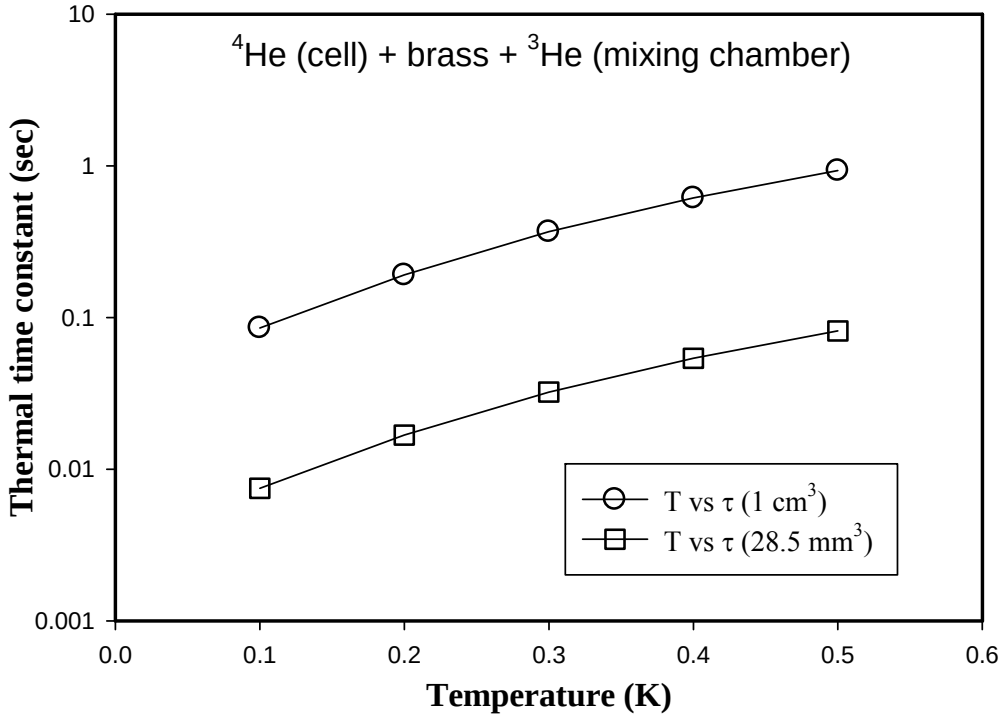

Figure 3.10: Thermal response time between Cu cell and mixing chamber with brass contact in between. τ increases significantly due to brass contact. The two plots are for different thermal resistance brass contacts.

solid ^{4}He (including Cu cell) and ^{3}He (in the mixing chamber). In this case, the required parameters for calculating thermal time constants are the heat capacities of solid ^{4}He and liquid ^{3}He and the thermal conductivity of brass. The experimental values of these parameters at 1.5 K are given in Table 3.4. Plugging these 1.5 K values in to the time constant formula gives a response time of 1 second for the smaller thermal resistance (0.5 mm × 6 mm × 9.5 mm) brass contact. The time constant is 12 seconds for the higher thermal resistance (1 cm × 1 cm × 1 cm) brass contact.

Material	Thermal property	Value
Liquid ^{3}He	Heat capacity	$C_V = 1.3794$ [J/K] [11]
Solid ^{4}He	Heat capacity	$C_V = 0.135$ [J/K] [40]
Brass	Thermal conductivity	$\kappa = 1.02[W/K.m]$ [39]

Table 3.4: Experimental thermodynamic values of C_V and κ for liquid ^{3}He, solid ^{4}He and brass at temperature 1.5 K.

Finally, we can say that the thermal response time for our system has been calculated numerically using empirical formulas and experimental values in the temperature range 100-500 mK and 1.5 K respectively. We obtained a response time of 10 milliseconds to 1 second in the temperature range of 100-500 mK and it depends greatly on thermal resistance of the contact (Figure 3.10). At 1.5 K, thermal response times are calculated to be 1.06 sec (0.5 mm thick) and 12 sec (1 cm thick) for the two brass contacts. This is usual since the thermal response time becomes slower with increasing temperature.

3.6 Thermal response time constant in our experiment

In this section we will use some of our experimental data to check the agreement between experimental thermal response times and the calculated values. Figures 3.11 & 3.12 show the experimental response time in the case of a 30.7 bar crystal using two brass thermal contacts of different dimensions. A thermal link (1 cm ×1 cm × 1 cm) identical to the one considered in our calculation has been used in the case of Figure 3.11. Although the response time calculated numerically for similar links is 12 seconds at 1.5 K; the real experimental values are quite

different. In the temperature range above 1.5 K this contact gives an experimental response time of around 75 seconds. This pulse was applied at 1.2 K with the heat pulse heater situated outside the cell.

In a later run of our experiment, thermal resistance of the brass contact was reduced 10 times by changing its dimension (6 mm × 9.5 mm × 0.5 mm). This results in faster quench cooling time of only 15 seconds as shown in Figure 3.12. This link gives a response time of 1 second at 1.5 K in numerical calculation. This time the heater was placed inside the Cu cell which allows the heat pulse to be applied to the solid ^{4}He internally. This calculated response time is also different from the experimental values.

The large discrepancy between calculated and experimental values can be explained in the following ways. The disagreement might be due to the fact that thermal properties like heat capacity and thermal conductivity of these materials change drastically with slight temperature change at low temperature. Another factor in this disagreement could be the response time of the thermometer (germanium resistance thermometer) we are using. In general, response time of a germanium resistance thermometer is around 200 msec at 4.2 K [34]. Moreover some part of the applied heat always reaches the mixing chamber (interrupting its cooling power), while applying heat pulses. This extra heat is not included in our calculation.

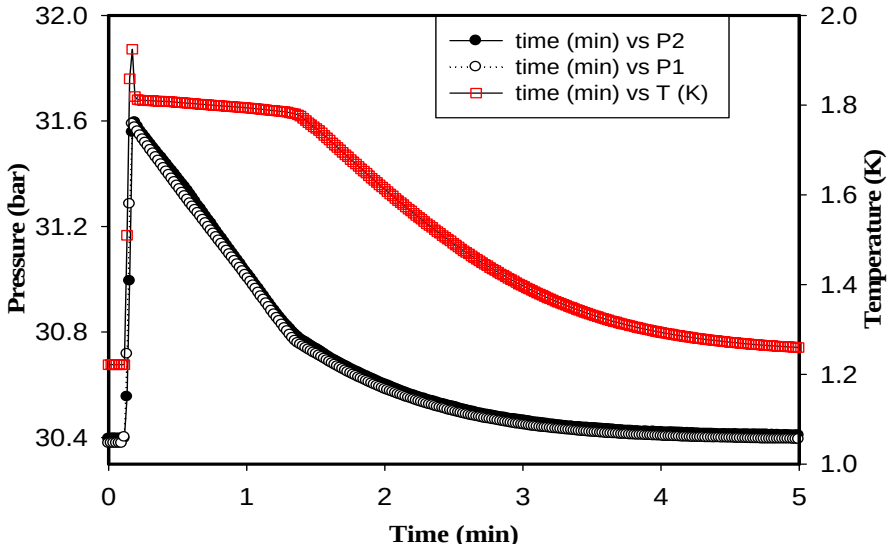

Figure 3.11: Thermal response time for the system in the case of brass (1 cm × 1 cm × 1 cm) contact with external heater. A thermal time constant value of 75 seconds has been found from the cooling after all liquid has frozen (at time around 1.5 minutes).

However, the most important parameter regarding this discrepancy is the contact resistance which is not included in our calculation [41]. The contact resistance in our experiment is the resistance due to the contact surface of the brass link with the Cu cell and the mixing chamber. It controls the effective resistance between the cell and mixing chamber. We can calculate the effective resistance either from Figure 3.11 or 3.12 in two different ways, using the melting percentage and latent heat of freezing or otherwise using the experimental response time and heat capacity.

As Figure 3.12 shows, 7.5% (discussed in chapter 4) of ^{4}He was melted by a 500 mJ heat pulse (internal heater) and this melted ^{4}He was cooled within 15 seconds. 7.5% of 0.27 mol of ^{4}He is 0.02 mol, which is 0.4 cm^3. Latent heat of

freezing of ^{4}He along the melting curve is 8.4 Jmol^{-1} [11]. Then the amount of heat needed to refreeze this 7.5% ^{4}He will be Q= 0.17 J. With a brass link (0.5 mm × 6 mm × 9.5 mm) in between, the heat was removed for 20 seconds to refreeze this melted ^{4}He. This requires a heat of 0.0085 J/s to be removed per second. Then the effective thermal resistance of the brass contact [R = ΔT/0.0085 J/s], linking the cell and the mixing chamber with a temperature difference ΔT= 1.2 K between them is 141 K/W. Similarly we can use the thermal time constant [τ = RC] of 15 seconds (Figure 3.12) to calculate the effective thermal resistance. Use of a heat capacity value of 0.135 J/K (Table 3.4) for solid ^{4}He gives an effective thermal resistance of 112 K/W. However, the original thermal resistance of the brass contact (6 mm × 9.5 mm × 0.5 mm) of Figure 3.12 is 9 K/W. Similarly, the effective thermal resistance for the bigger thermal link (1 cm × 1 cm × 1 cm) can be calculated from Figure 3.11.

We believe this large effective thermal resistance is coming from the contact resistance between the brass link with the cell and the mixing chamber. The accurate value of the contact resistance between two pressed contacts is very difficult to calculate. It depends on the pressing force between the contacts rather than on the contact surface area. The discrepancy between our calculated and measured time constants might be reduced by clamping the surfaces very tightly.

However, we did the numerical calculations to estimate the thermal time constant of our whole system. Despite the discrepancy, these ideas allow us to get

reasonable control over the quench cooling time of our experiment. This permits us to quench cool our sample fairly rapidly, sometimes in as little as 15 seconds.

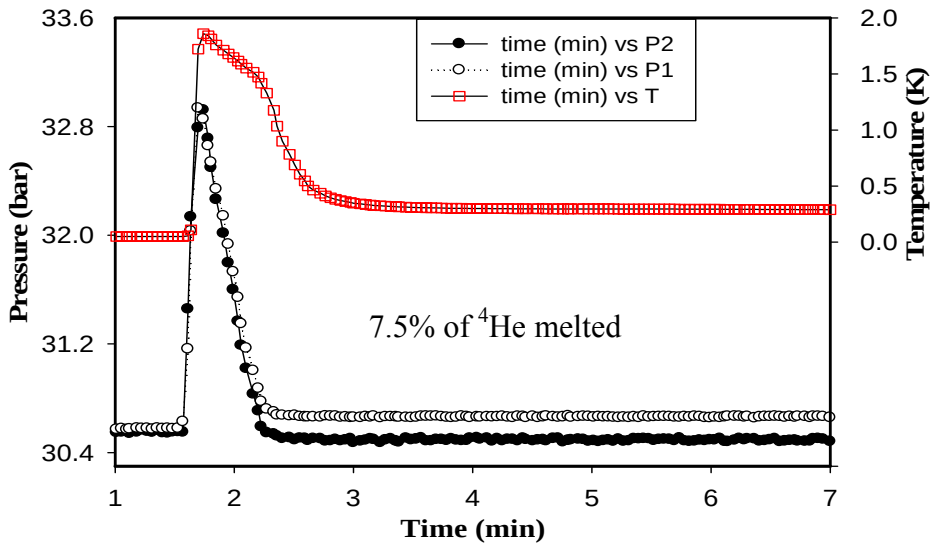

Figure 3.12: Thermal response time for the system in the case of a lower thermal resistance brass (6 mm × 9.5 mm × 0.5 mm) contact with internal heater. A response time value of 15 seconds has been found.

In this chapter, a brief description of our dilution fridge along with the temperature and pressure measurement devices has been provided. A description of our crystal growing technique has been given with additional information on the method to create more defects in the crystal. The thermodynamic properties of materials have been summarized for the calculations. Using this knowledge, we are able to control the response time of our system and hence the quench cooling time.

Chapter 4

Results

This chapter will discuss the results of our experiment. The measurements taken in this experiment involve pressure, temperature and time. We analyzed our pressure measurements to study pressure-temperature equilibrium, pressure gradients and annealing of crystals. Energy of thermal activation of defects is calculated from pressure relaxation data. Moreover, some brief discussion about disordered (two level) systems and their relevance to helium crystals will be provided, along with discussion of the difficulties that arise in extracting thermodynamic information from pressure data.

4.1 Pressure gradients in solid helium crystals

The blocked capillary method growth introduces large pressure gradients in crystals. Since all our crystals are made using this method, a noticeable pressure gradient is produced. We have grown several crystals in the pressure range from 26 – 44 bar. The typical pressure gradient produced just after growth is ~30 mbar and this remains all the way to the lowest temperature.

Blocked capillary growth of crystal is shown in Figure 4.1. We have plotted the pressure at one end of the cell for several crystals. All crystals follow the melting curve during growth. The pressure at the other end of the cell is plotted in Figure 4.2, where the melting curve of ^{4}He is also shown for comparison. One of our lower pressure crystals (Crystal_Dec07_2009_28.5 bar_ initial cooling)

passes through the bcc/hcp mixed phase. This can be seen by plotting this 28.5 bar crystal's pressure along with the melting curve and is shown in Figure 4.3. This figure shows that the crystal leaves the melting curve at 1.78 K and then stays on the bcc/hcp coexistence line until it enters the pure hcp phase at around 1.6 K. Pressure gradients created by the growth method become visible if the pressures at both ends of the crystal are plotted against temperature, as in Figure 4.4. A pressure difference of 30 mbar is clearly visible just after growth (heater was embedded in solid helium) and it remains even at the lowest temperature unless some annealing is done. Annealing at higher temperature reduces this gradient. Figure 4.4, also shows evidence of some pressure gradient along the melting curve (right axis) just before complete freezing. This is obvious, as freezing

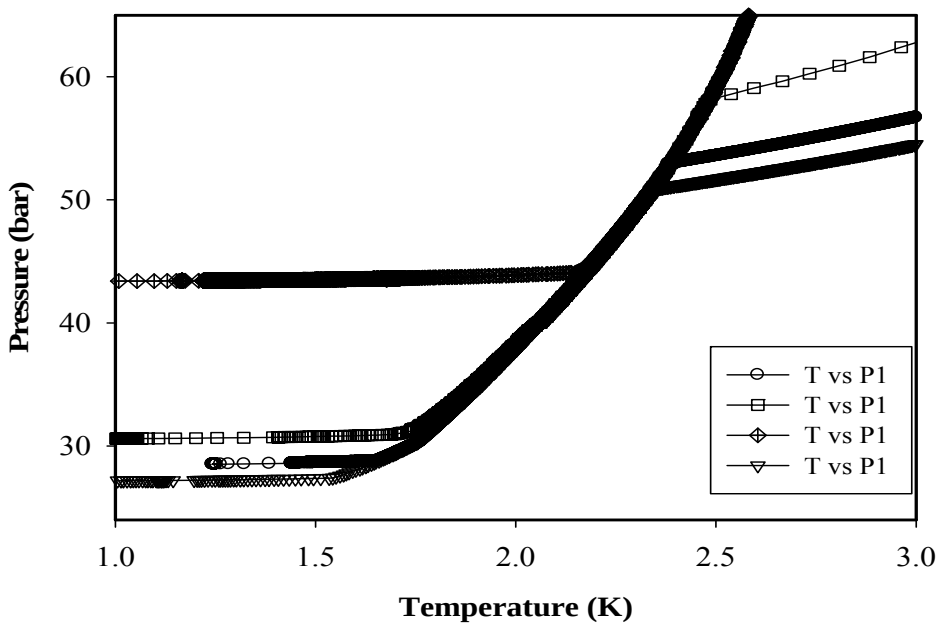

Figure 4.1: Blocked capillary growth of solid helium crystals. Only one end pressure of the cell (P1) is plotted for simplicity.

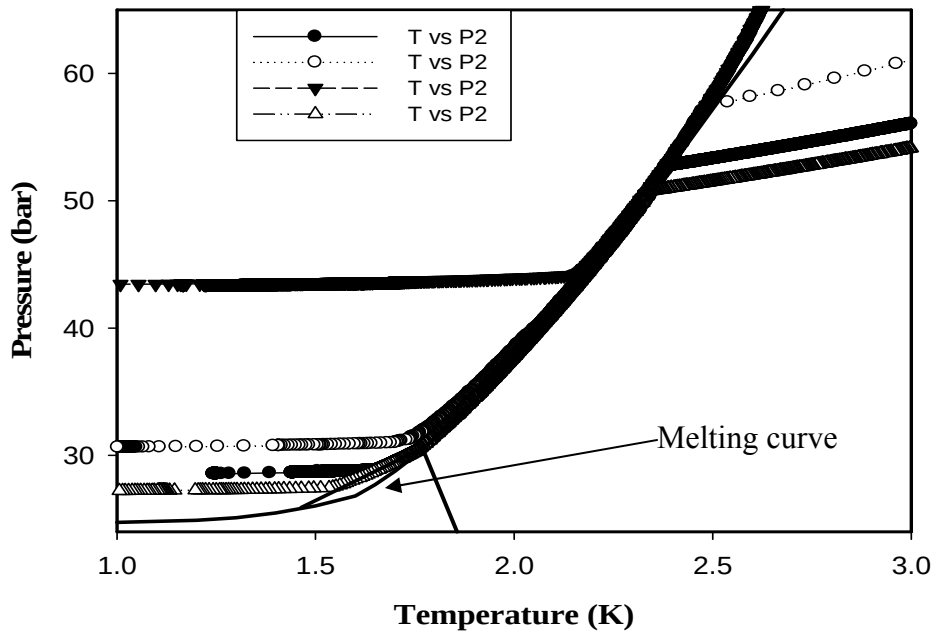

Figure 4.2: Blocked capillary growth of solid helium crystals. Only one pressure of the cell (P2) is plotted for simplicity. The melting curve is also shown in this curve.

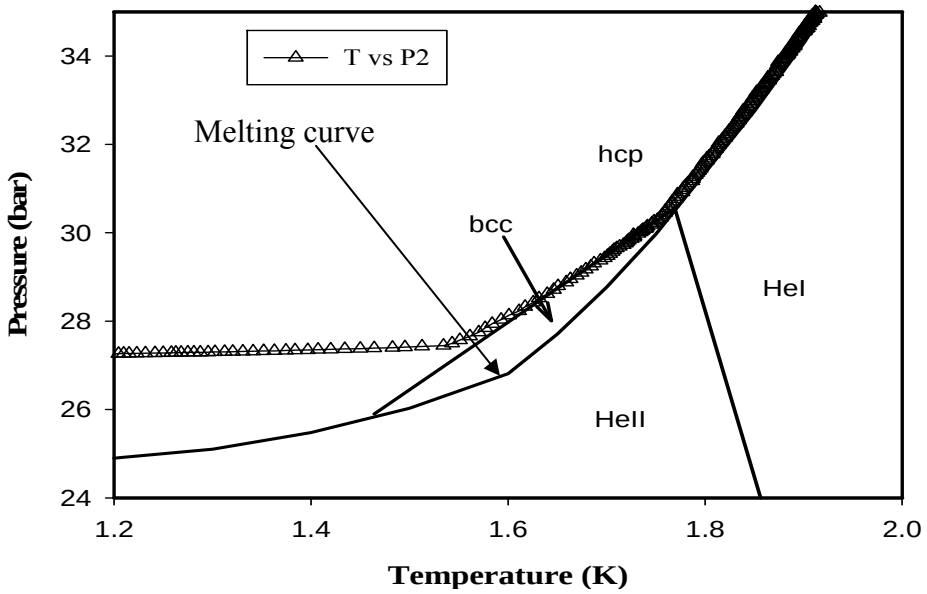

Figure 4.3: One end pressure of a lower pressure crystal (Crystal_Dec07_2009_28.5 bar_ initial cooling) is plotted with the melting curve to show the crossing through the bcc/hcp mixed phase. This crystal enters the pure hcp phase at around 1.6 K.

always starts from the end closest to the mixing chamber and then continues along the cell for complete freezing.

However, we have rapidly heated crystals to produce large temperature gradient which increases the pressure gradients. After that they were cooled rapidly to low temperature to avoid annealing of these gradients. Crystals were also partially melted and quench cooled where the change in volume during the melting introduces a large change in crystal pressure and hence in gradient. Both approaches result in a significant rise in pressure gradients in the crystal. Partial melting of a crystal (Crystal_Nov10_2009_31 bar_500 mJ heat pulsed) using heat pulses is shown in Figure 4.5 in a pressure temperature plot (internal heater). The

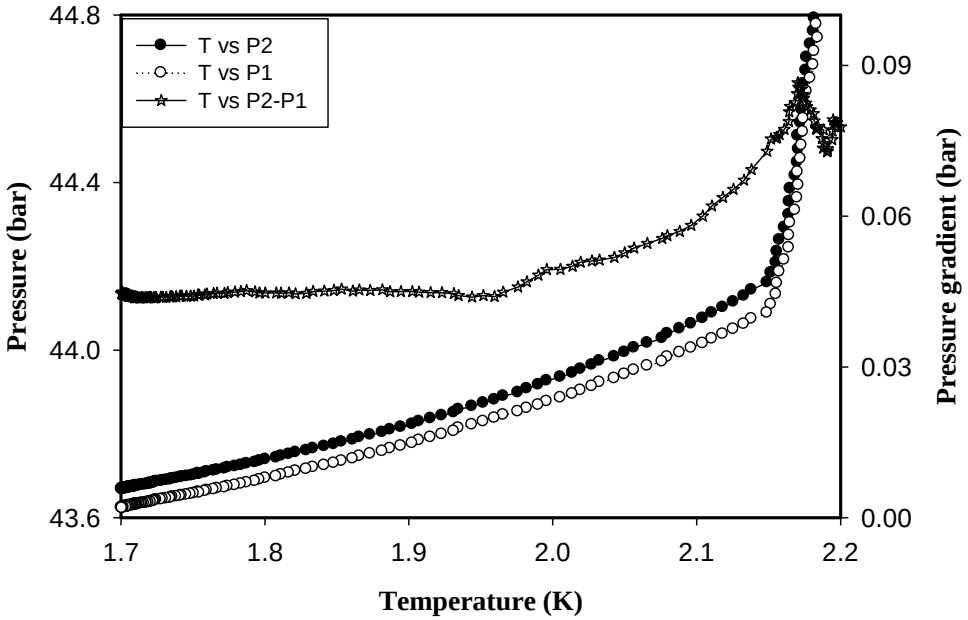

Figure 4.4: Pressure gradient (internal heater) of around 30 mbar introduced during blocked capillary growth. Data is shown in the case of 28.8 bar crystal (Crystal_Oct30_2009_28.8 bar_ initial cooling). The left axis shows the two ends pressure and the right axis shows the pressure difference.

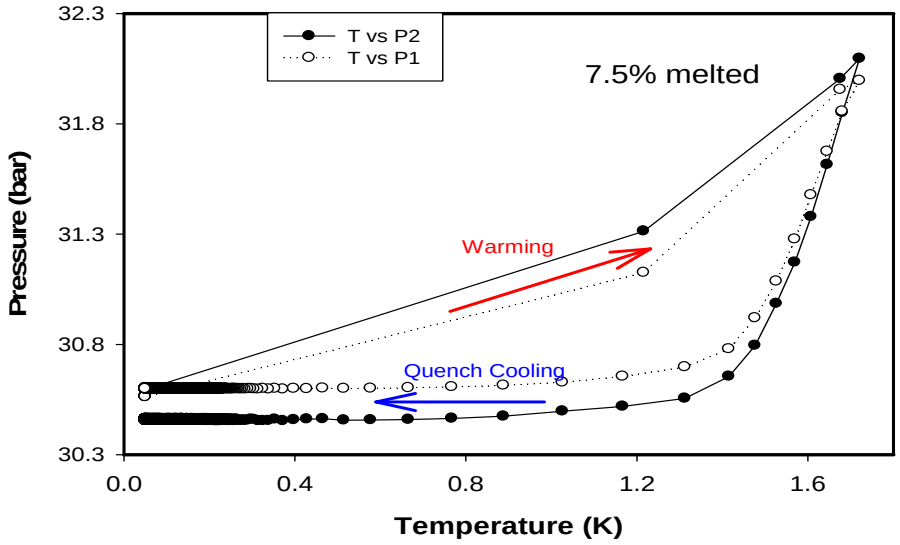

Figure 4.5: Partial melting by a 500 mJ heat pulse with both end's pressure plotted. Due to the pulse (internal heater), crystal (Crystal_Nov10_2009_31 bar_500 mJ heat pulsed) pressure reaches the melting curve, follows it and then leaves the curve after refreezing. 7.5% melting of crystal raises the pressure gradient during the process.

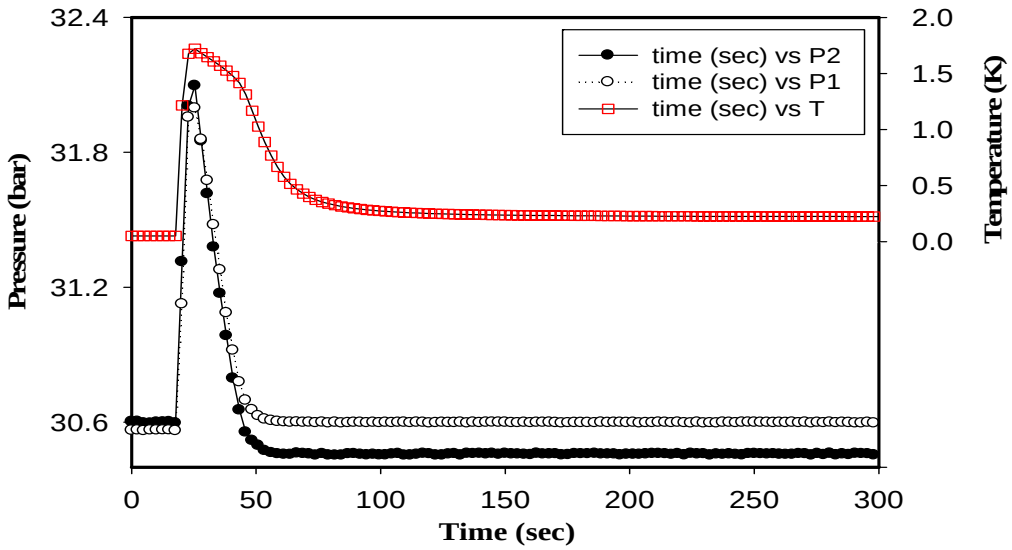

Figure 4.6: Increase of pressure gradient by a 500 mJ heat pulse (internal heater) is shown. 7.5% melting of the crystal (Crystal_Nov10_2009_31 bar_500 mJ heat pulsed) raises the gradient to 160 mbar.

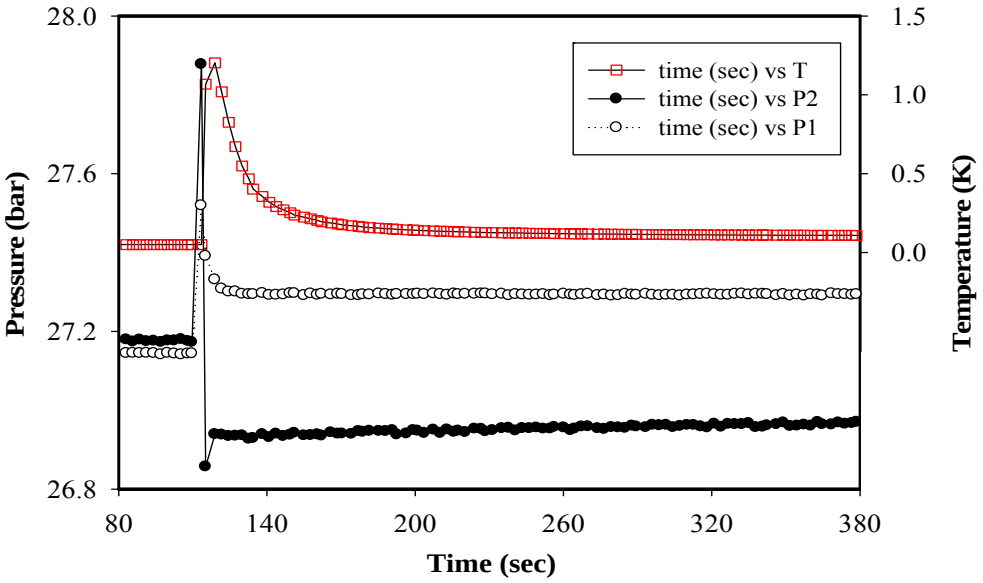

Figure 4.7: A pressure gradient of 330 mbar is produced by a small pulse (internal heater) of 100 mJ. The crystal (Crystal_Dec07_2009_28.5 bar_100 mJ heat pulsed) was thermally quenched with 0% of it being melted.

percentage of solid ^{4}He melted with a 500 mJ heat pulse is 7.5%. This percentage was calculated using Figure 3.5, which shows that growth of crystal creates a pressure change of around 20 bar along the melting curve. This 500 mJ heat pulse produces a pressure change of 1.5 bar which gives the 7.5% melting percentage.

An increase in pressure gradient by partial melting and thermal quenching of a crystal is shown in both Figures 4.5 & 4.6. A 500 mJ heat pulse melted 7.5% of the crystal (Figure 4.6) and generated a pressure gradient of 160 mbar. Initially there was only a small gradient of 30 mbar present in the crystals, introduced by the growth method but melting produced by the heat pulse raised the gradient to 160 mbar.

As shown in Figure 4.7, even larger gradients can be produced in a crystal (Crystal_Dec07_2009_28.5 bar_100 mJ heat pulsed) by smaller pulses. A 100 mJ heat pulse (internal heater) produced 330 mbar of gradient without melting any solid helium (the initial gradient was also 30 mbar). The reason for this large gradient produced by a small pulse is a phase transition in the crystal during the heat pulse. This hcp crystal passes through the bcc/hcp mixed phase (Figure 4.3) just after growth. In response to the heat pulse, it again enters then leaves the mixed phase. These phase transitions give rise to the larger pressure gradient.

In most cases, pressure differences produced by heat pulses are in the range 200 – 250 mbar. Since pressure gradients in a crystal determine amount of stress in it, an estimate of yield stress of the crystal can be made. The exact relationship between stress and pressure difference depends on the geometry of the cell. In the case of our open cylindrical cell a yield stress of the order of 100 mbar was estimated.

4.2 Cooling and warming of crystal

Crystals were warmed and cooled both at high and low temperature and the thermodynamic (P vs. T) paths were measured. Just after growth, crystals were warmed and cooled near the melting temperature. This affected the melting onset of the crystal. A sharper onset was found in the case of warming.

During growth, a pressure gradient was produced in the crystal. This gradient decreased if the crystal was warmed to melting temperature. This is due to annealing. Figure 4.8 shows such cooling followed by warming for a 30.7 bar

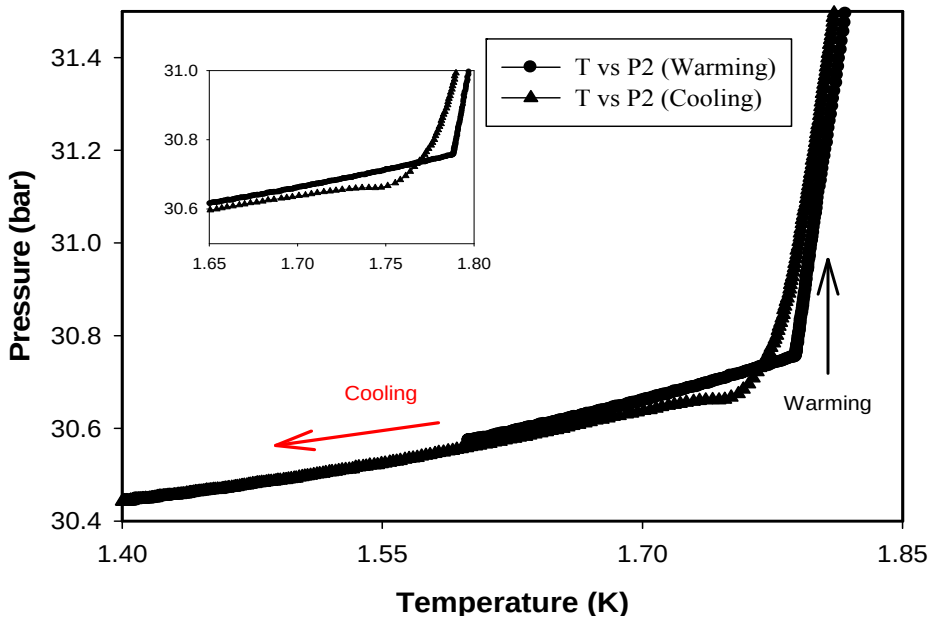

Figure 4.8: One end pressure (P2) of the crystal (Crystal_July24_2009_30.7 bar_ Ramp down & up (1.6-1.85 K)) is plotted vs temperature for both cooling & warming (external heater) near melting temperature.

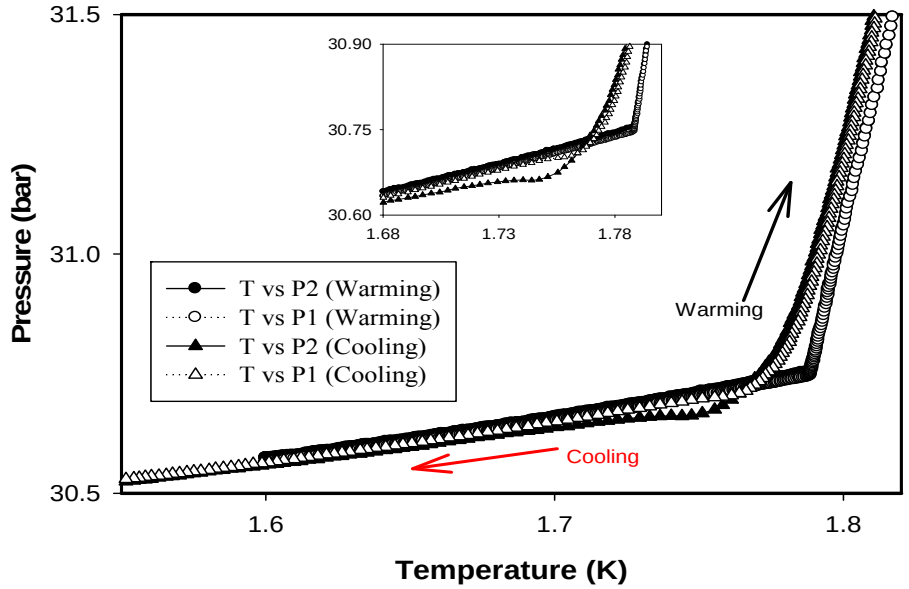

Figure 4.9: Both pressure gauges are plotted against temperature to see gradient & onset of melting in the case of cooling and warming (external heater) of crystal (Crystal_July24_2009_30.7 bar_ Ramp down & up (1.6-1.85 K)).

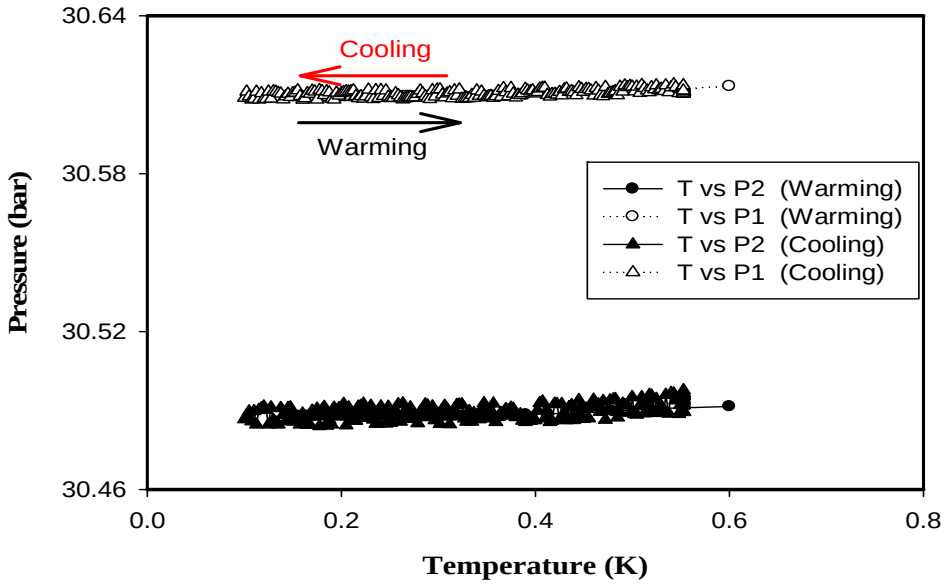

Figure 4.10: Cooling and warming (internal heater) of crystal (Crystal_Nov10_2009_31 bar_512 mJ heat pulsed) follows the same thermodynamic path at both ends. No hysteresis was observed.

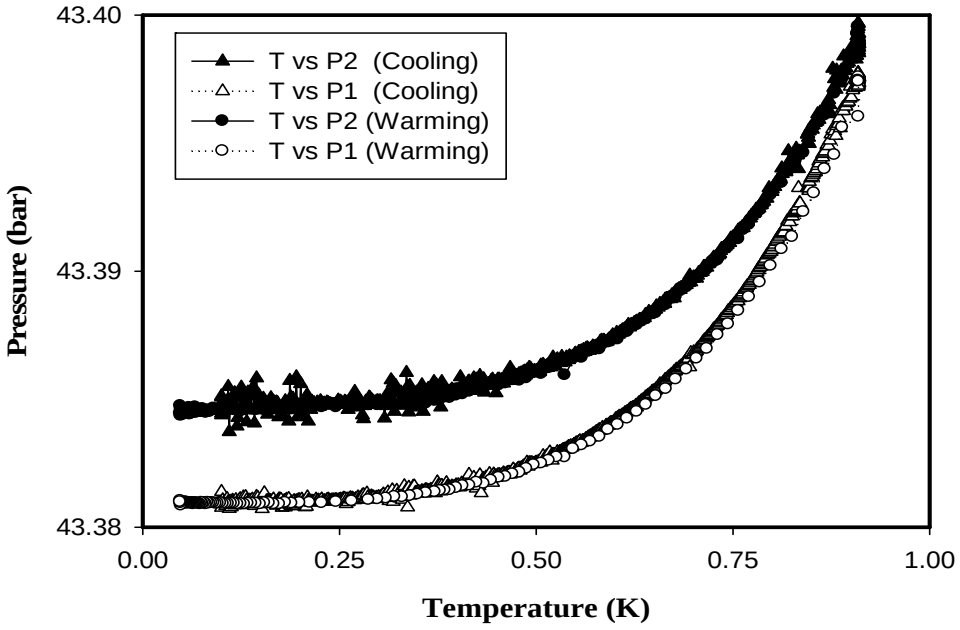

Figure 4.11: Similar cooling and warming (internal heater) characteristic was observed in the case of a higher pressure crystal (Crystal_Nov27_2009_43.5 bar_ second annealed). Pressure at both ends of the cell is plotted.

crystal. Warming almost eliminates the pressure gradients, and the melting onset is sharp. Reduction of the pressure gradient is shown in Figure 4.9 where the pressures from both gauges are plotted against temperature.

However, no significant changes in pressure were observed during cooling and warming at low temperature. The pressure at low temperature follows the same thermodynamic path during cooling and warming. As shown in Figure 4.10, a 31 bar crystal was cooled and warmed in the temperature range 100 – 600 mK. Both pressure gauges record similar temperature dependences and no hysteresis was observed. Figure 4.11 shows the absence of hysteresis in a high pressure 43.5 bar crystal during cooling and warming in the temperature range 50 – 900 mK.

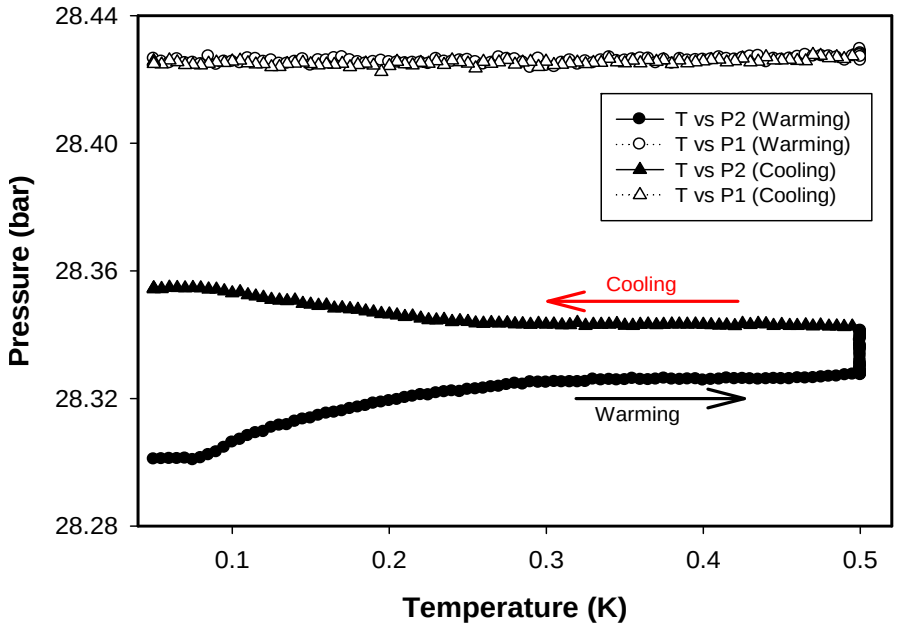

Figure 4.12: An example of crystal (Crystal_Oct30_2009_28.8 bar_ heat pulsed) pressure following different thermodynamic path during warming (internal heater) and cooling is shown. Difference in thermodynamic path is observed only in the heater end (P_2) of the crystal.

Unusual behavior was observed in the case of a 28.8 bar crystal (Figure 4.12). In all other crystals a similar pressure response was observed- pressure goes down with decrease in temperature- but this low pressure crystal shows the opposite behavior in the case of cooling from 500 mK.

Initially the crystal was warmed up from 50 to 500 mK in 9 hours, followed by annealing at 500 mK for 3 hours. During this time the crystal exhibited normal behavior; pressure went up with the rise in temperature. Then the crystal was cooled to 50 mK from 500 mK in another 9 hours. Cooling showed the opposite pressure response at one end (P_2) of the crystal. However the pressure at the other end remained unchanged during warming and cooling. After warming and cooling an overall pressure rise of 50 mbar was found at one end. The reason for this rise is unknown.

4.3 Annealing of crystal

We introduce pressure gradients in crystals during the growth process and these could be increased (up to about 330 mbar) with plastic flow from heat pulses. These gradients create defects in the crystals. All the crystals were studied at low and high temperatures. After creating defects by heat pulses, crystals were kept at 50 mK temperature to look for pressure relaxation at low temperature [42]. Figure 4.13 shows a pressure relaxation plot for a 31 bar crystal. Initially a 150 mbar pressure gradient was produced in the crystal and then it was kept at 50 mK for 17 hours to look for pressure relaxation. During this 17 hour period no change in pressure was observed. A small relaxation of 0.1 mbar was seen at 19 mK [42]

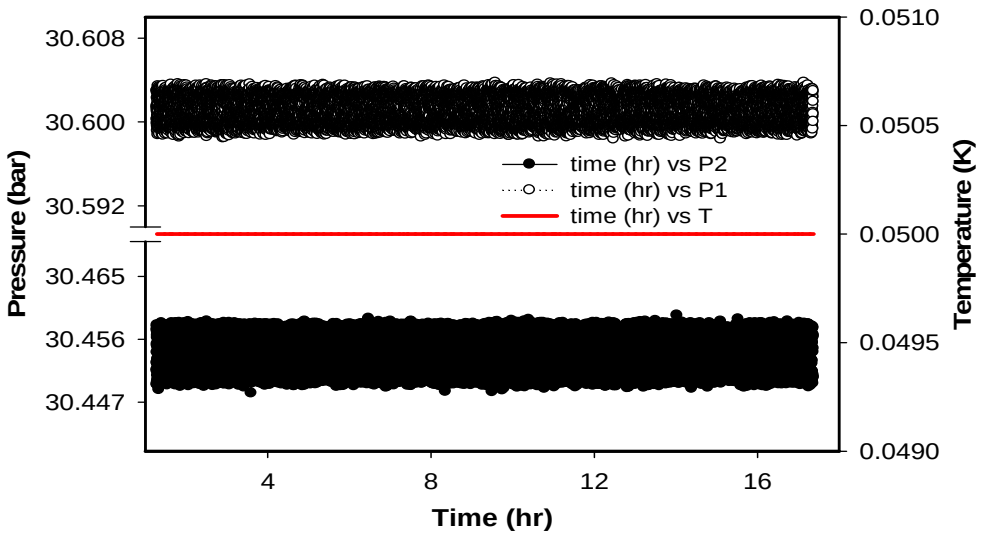

Figure 4.13: Pressure relaxation of two gauges at 50 mK is plotted (internal heater) against time in the case of a 31 bar crystal (Crystal_Nov10_2009_31 bar_ heat pulsed). Temperature (line) is plotted on the right axis.

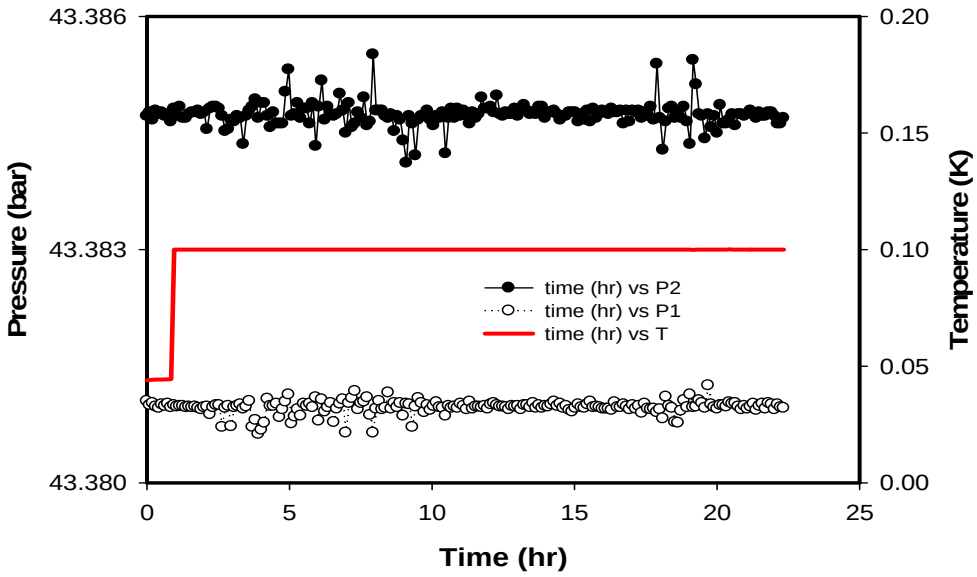

Figure 4.14: Pressure relaxation of an annealed (internal heater) crystal (Crystal_Nov27_2009_43.5 bar_ second annealed) at 100 mK is plotted. Temperature is plotted on the right axis for clarity.

temperature in a previous experiment. This absence of pressure relaxation in our experiment might be due to the smaller sensitivity of our pressure gauges.

Similarly no pressure relaxation was observed in the case of an annealed crystal (Figure 4.14). After annealing up to 1.6 K, the remaining pressure gradient in the crystal was around 4 mbar. Then the crystal was cooled to 100 mK and kept there for 22 hours during which time no visible pressure relaxation was seen. Thus either our pressure gauges are not sensitive enough or there is no relaxation at low temperature. Further experiments are needed with more sensitive gauges.

However, annealing was observed at higher temperature in crystals with large pressure gradients. A crystal (Crystal_Nov27_2009_43.5 bar_750 mJ_ heat pulsed) with a pressure gradient of 240 mbar was warmed up to 1.6 K in a 29 hour period with a rate of 0.85 mK/minute. This warming of the crystal reduces its pressure gradients due to annealing at higher temperature. After that, the crystal was cooled to the base temperature. The pressure gradient left in the cooled crystal was almost zero due to high temperature annealing. Figure 4.15(a) shows the pressure at both ends of the crystal to illustrate this change in gradient. Most of the reduction in pressure gradient occurs at temperatures above 0.8 K. Response in average pressure during the warming and cooling of crystal is shown in Figure 4.15(b). This shows that, cooling after annealing results in a rise in average pressure of the crystal which might be caused by a slip on solid plug in the cell capillary during annealing.

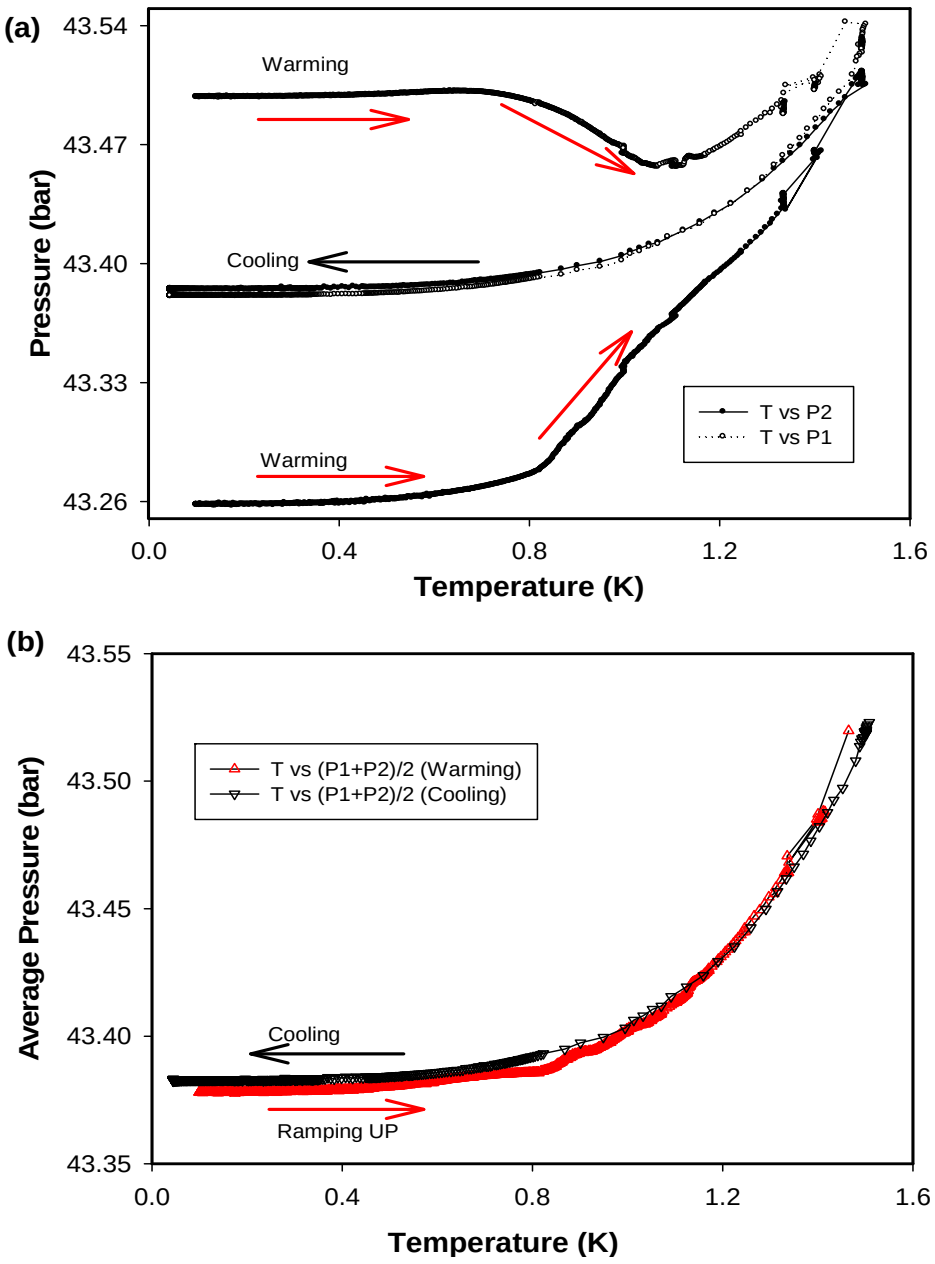

Figure 4.15: Pressure temperature response of a crystal (Crystal_Nov27_2009_43.5 bar_750 mJ_ heat pulsed) during annealing (internal heater) and cooling (after annealing) is plotted. (a) Reduction of the pressure gradient results in the two pressures falling almost on the same curve during cooling (after annealing). (b) Average pressure during warming and consecutive cooling is plotted.

Annealing can be understood in more detail from Figure 4.16 where the pressures at the two ends of a 31 bar crystal, and the temperature, are plotted against time. A pressure gradient of 260 mbar was introduced in this crystal with a 730 mJ heat pulse. The crystal was then warmed from 50 mK in 50 or 100 mK

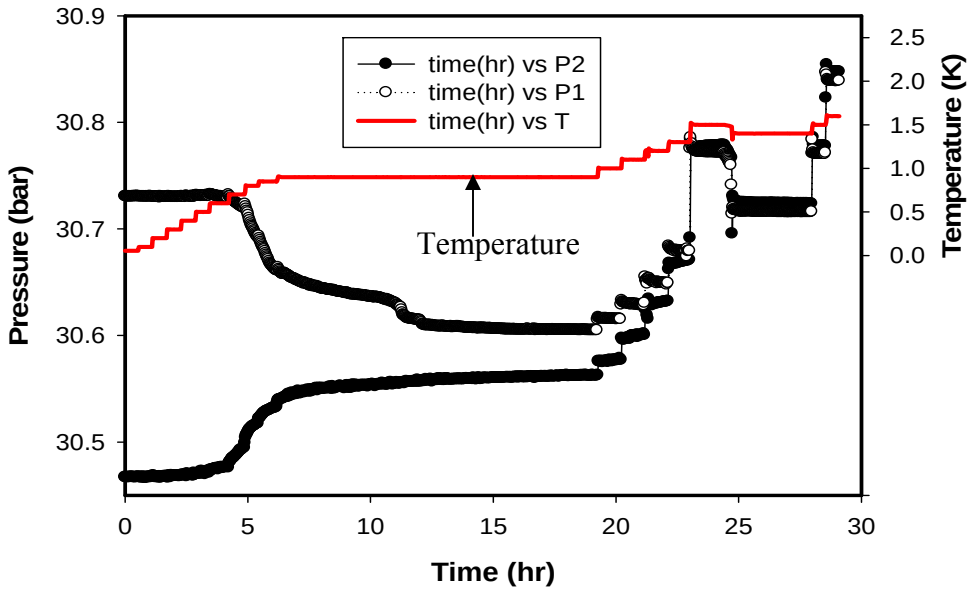

Figure 4.16: Annealing (internal heater) data of crystal (Crystal_Nov10_2009_31 bar_730 mJ heat pulsed) is plotted for 29 hour period. Temperature and the pressure at the two ends of the crystal are plotted as a function of time. During annealing, the crystal pressure behaves differently at each end until they become stable.

steps. It was kept at each temperature for 1 hour to look for annealing. Significant annealing of the crystal started at the 4th hour at around 500 mK. We continued this stepwise annealing up to 900 mK and then stayed at 900 mK for 13 hours. During these 13 hours of annealing, the crystal's pressure stabilized but still a pressure difference (P1-P2) of 40 mbar was left.

The crystal was further warmed to 1.6 K in 100 mK steps to get rid of the remaining pressure difference. At 1.3 K, the pressure difference (ΔP) goes to zero and after that it changes sign. Figure 4.17 shows the same annealing data but plotted as the average pressure ($(P_1+P_2)/2$) and difference in pressure (P_1-P_2) against time. This plot shows that the average pressure of the crystal does not

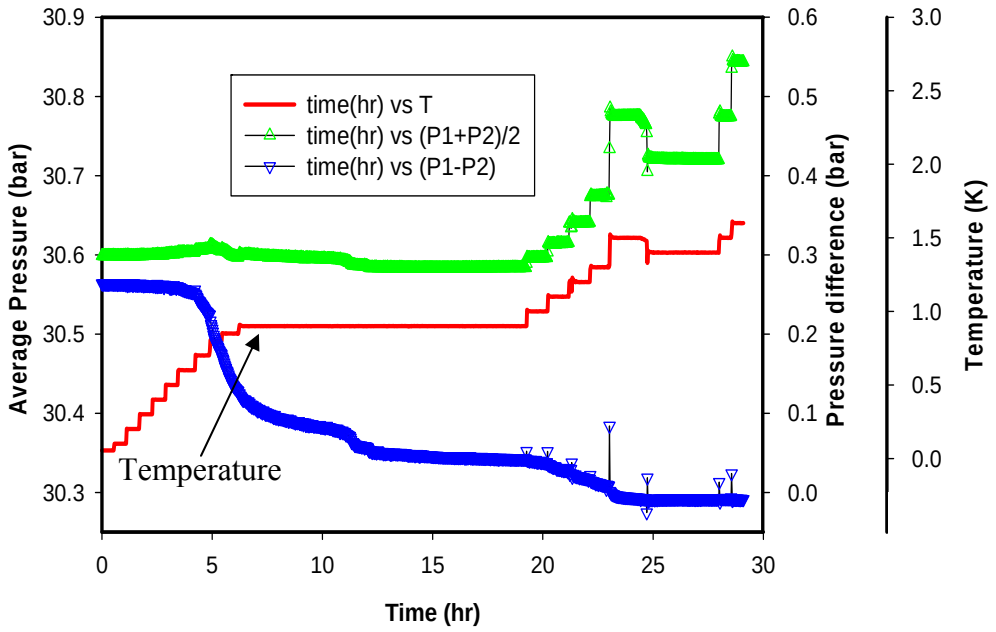

Figure 4.17: Average pressure (upward triangle), pressure difference (downward triangle) and temperature (line) of a 31 bar crystal (Crystal_Nov10_2009_31 bar_730 mJ heat pulsed) are plotted with time. Reduction of gradient is visible in the plot whereas average pressure remains nearly unchanged during annealing (internal heater).

change a lot during annealing. Figure 4.17 shows that the average pressure (upward triangles) remains almost the same during the first 19 hours of annealing. In later annealing of the crystal, the average pressure simply follows the thermodynamic temperature dependence.

The reduction in pressure gradient is very clear in Figure 4.17. The pressure difference (downward triangles) plotted in this figure starts dropping during the 4^{th} hour of annealing at around 500 mK. In the first four hours, there was some annealing but it was insignificant. The pressure gradient reduces to zero at 1.3 K after 23 hour of annealing, further annealing changes the sign of the pressure difference showing there are still some pressure inhomogeneities in the crystal. And, $\Delta P = 0$ corresponds to equal pressure at the ends where measurement is being conducted but the inhomogeneous pressure may stays at any points other than the two ends. The final pressure difference on this crystal after 29 hours of annealing was -8 mbar and as the annealing proceeds, ΔP tends to be more negative. Thus annealing does not completely remove pressure gradients; this is not surprising as we cannot get rid of all the defects by annealing.

Annealing data in the case of a higher pressure crystal also shows similar behavior. The annealing of a 43.5 bar crystal over 33 hours is shown in Figure 4.18. The average and difference in pressure for this crystal are shown in Figure 4.19. Annealing at 1.3 K removed almost the entire pressure gradient. The melting temperature of this crystal is 2.17 K. Thus annealing reduces pressure gradients but leaves the average pressure more or less unaffected.

As Figure 4.16 and 4.18 show, the annealing started at around 500 mK but the pressures at the two ends behave differently as annealing proceeds. The pressure (P_1) at one end of the crystal goes down with annealing whereas the other

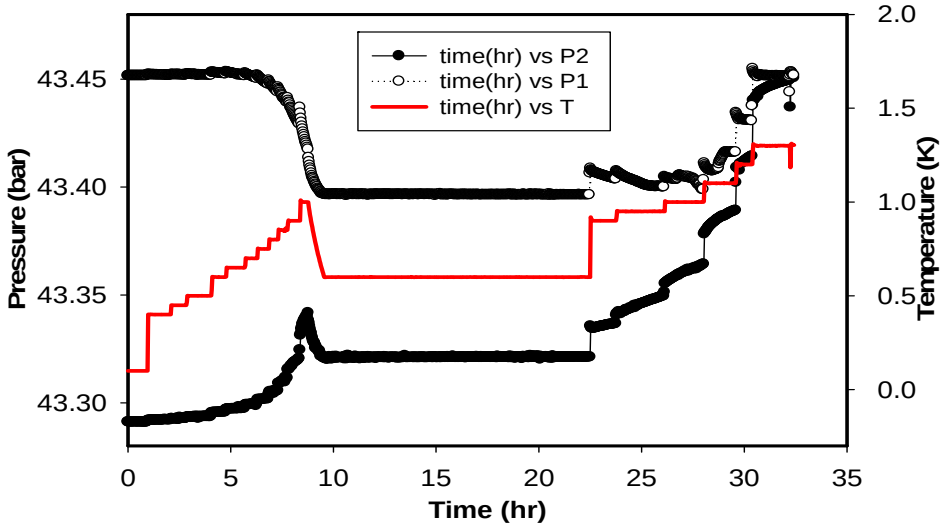

Figure 4.18: Annealing data for a higher pressure (43.5 bar) crystal (Crystal_Nov27_2009_43.5 bar_750 mJ_ heat pulsed). The two end pressure changes in an opposite manner as annealing (internal heater) proceeds until they become stable. After that the pressure simply follows thermodynamic temperature.

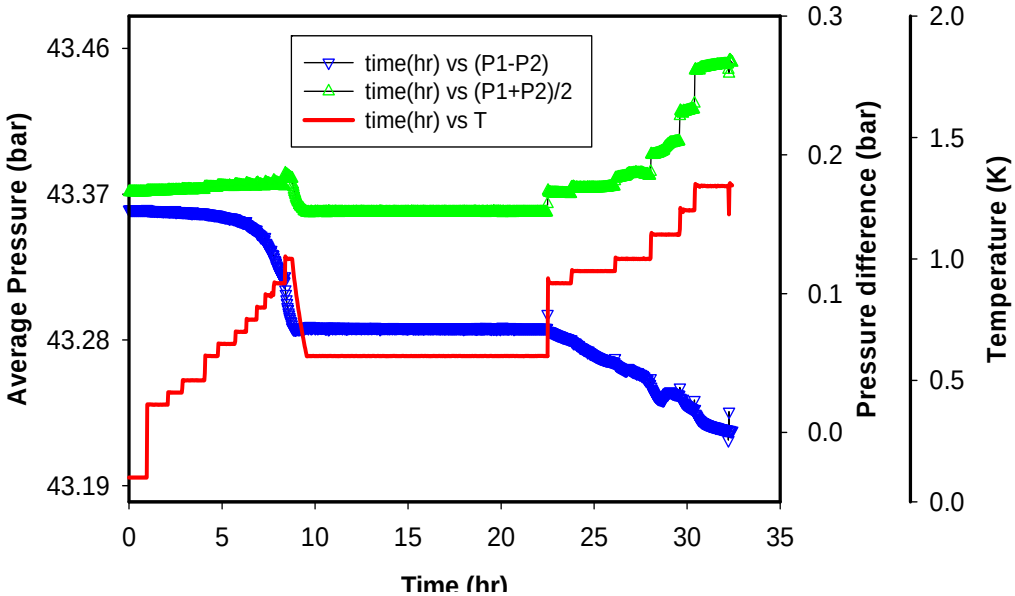

Figure 4.19: Removal of pressure gradient by annealing (internal heater) is shown in 43.5 bar crystal (Crystal_Nov27_2009_43.5 bar_750 mJ_ heat pulsed). 33 hour annealing makes the gradient (downward triangle) zero with very little change in crystal's average pressure (upward triangle). Temperature (line) is changed in a stepwise manner.

end's pressure (P_2) goes up. The P_2 end is where the temperature control and heat pulse heaters are connected. It is clear that a single pressure gauge is not sufficient to characterize the pressure in a crystal because the pressure in a crystal is not uniform and may have different behavior at different points in the cell, as is shown in Figure 4.16 and 4.18. More than one pressure gauge is needed and the average of these gauges may provide a pressure value which is more useful than one obtained with a single gauge.

4.4 Activation energy

We have learned that annealing of solid ^{4}He crystals reduces the pressure gradient. This occurs by thermal activation. The more the temperature rises, the faster the annealing rate becomes until the pressure stabilizes. We can use the annealing rate to determine the energy of the thermal activation process using the Arrhenius formula given in equation 2.17.

To calculate activation energy we must know how the rate of a process depends on temperature. This can be found using annealing plots of the type shown in Figure 4.18. In this plot, annealing is shown for a 43.5 bar crystal for a period of 33 hours. Figure 4.20 shows an enlarged plot (for the annealing of 43.5 bar crystal) of the temperature region where most of the annealing occurs. From Figure 4.18, it is clear that most of the annealing occurs between 3 and 8 hours, in the temperature range 500 – 900 mK. Figure 4.20 shows that starting from 500

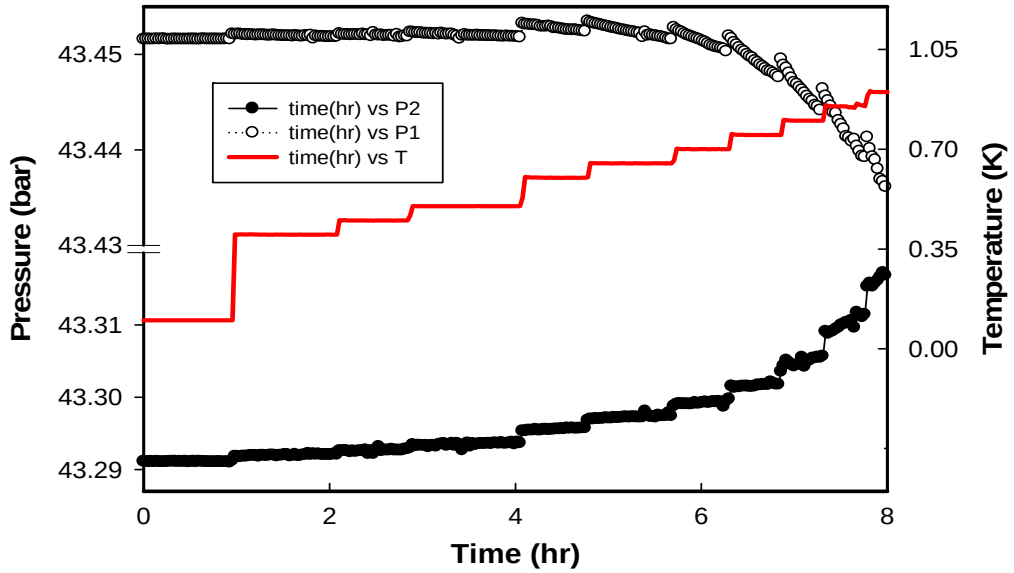

Figure 4.20: A blown up plot for the annealing of a crystal (Crystal_Nov27_2009_43.5 bar_750 mJ_ heat pulsed). Most of the annealing is done in the temperature range 500-900 mK. Annealing rate at each temperature can be calculated using the slope of each of the straight line segments (pressure vs. time) at that temperature.

mK, as the temperature rises the annealing rate become faster (the slope of pressure curve is steeper). The slope of this pressure versus time curve gives the rate of pressure relaxation. For example, the rate of annealing at 800 mK can be obtained from the slope of a pressure (P_1) vs. time plot as shown in Figure 4.21. Rates at other temperatures can be determined in the same way. Sometimes, the rate of change in pressure is not quite linear just after raising the temperature. We then, wait for several minutes for the pressure change to become linear and then calculated the rate.

If the inverse of temperature (1/T) is plotted versus the logarithm of the rate (i.e., the slope) then, according to equation 2.18, slope of this plot will give the

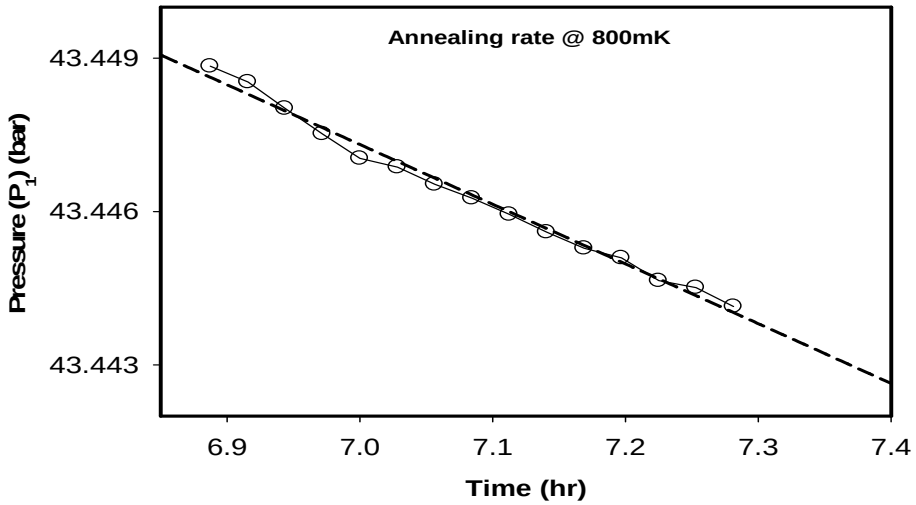

Figure 4.21: Pressure variation with time at 800 mK for the 43.5 bar crystal (Crystal_Nov27_2009_43.5 bar_750 mJ_ heat pulsed). Rates of relaxation can be figured out from the slope of this linear pressure-time curve.

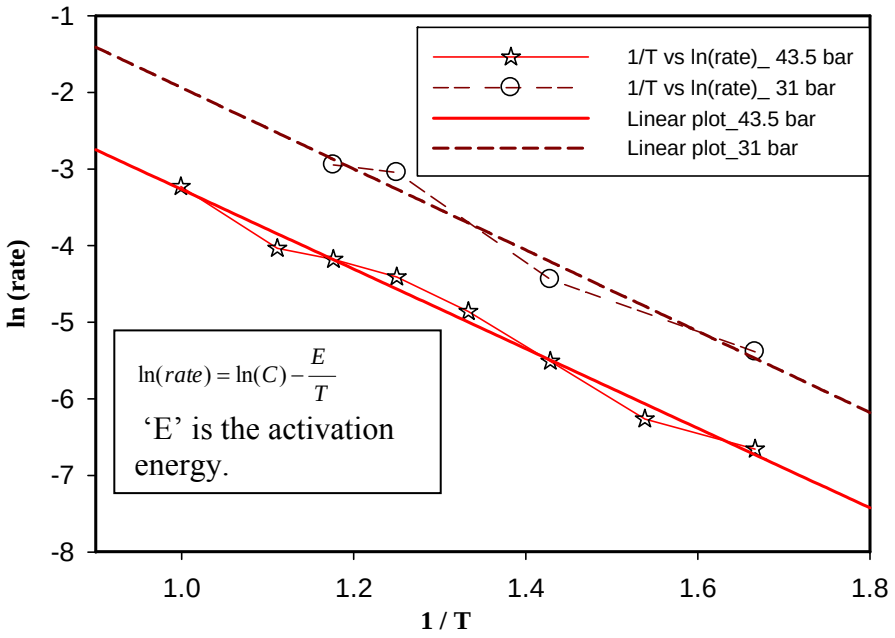

Figure 4.22: Arrhenius plot to find activation energy of annealing. The energy calculated is 5.1 K for a 43.5 bar crystal (Crystal_Nov27_2009_43.5 bar). A value of 5.0 K is found in the case of a 31 bar crystal (Crystal_Nov10_2009_31 bar_730 mJ heat pulsed). Straight lines are fitted to the curves to find the slopes which give the activation energies for the temperature range 600 – 1000 mK.

activation energy of the thermal process. This gives an activation energy of 5.1 K for our 43.5 bar crystal of Figure 4.20. This is shown in Figure 4.22 (points indicated by stars). We have also measured the activation energy of a 31 bar crystal, which gives a similar value of 5.0 K (shown in Figure 4.22 by empty circles). Therefore the activation energy of the thermal process responsible for the pressure change between 0.6 K and 1.0 K in solid ^{4}He is about 5 K. We can also calculate this activation energy using the rate of change of pressure (P_2) at the other ends of crystal or otherwise using the difference in pressure between the two ends.

Defects like vacancies and dislocations thermally activate in different temperature regions in solid ^{4}He crystals. At low temperature (below 200 mK) dislocations become pinned by ^{3}He impurities, which gives the stiffening in shear modulus of solid ^{4}He. A rise in temperature thermally unbinds the dislocations (from the ^{3}He pinning) with an activation energy of 0.7 K [43]. This occurs at around 200 mK and then the dislocations can move freely. However, this annealing of dislocations requires mass transport which is initiated by thermal hopping of atoms in the presence of vacancies. The activation energy we have found in our pressure measurements is 5 K in the temperature range 0.5-1.0 K. Our calculated activation energy must be of something other than the unbinding of ^{3}He impurities from dislocations.

On the other hand, vacancies in ^{4}He crystals disappear at low temperature and start to appear thermally as temperature rises. Several experimental studies

determined the activation energy of vacancies. NMR [44], X-ray [45] and neutron scattering [46] measurements give a value of around 10 - 11 K for crystals with molar volume 20-20.9 cm^3. Theoretical studies also give a vacancy activation energy of 10-15 K [47]. The activation energy we have calculated from our measurement is around 5 K, which is about half the measured value for vacancies. However, our value is close to that obtained by a different group [48] in their pressure measurement. Vacancy motion may be responsible for the annealing of pressure gradients we see in solid ^{4}He, even though the activation energy (5 K) is smaller than the vacancy energy from most other measurements. It is possible, for example, that annealing of dislocations involves vacancies moving along dislocation cores ("pipe diffusion") with smaller activation energies than in bulk solid helium.

4.5 Pressure temperature dependence

An initial goal of our measurement was to find the equilibrium temperature dependence of the pressure at low temperature. This dependence could reveal the existence of two level systems in solid ^{4}He. We tried to find a quadratic (T^2) coefficient in the pressure temperature dependence formula (as discussed in chapter 2) for all our crystals. Though it is easy to measure the Debye T^4 coefficient, we found no clear sign of a T^2 coefficient. Figure 4.23 shows the initial cooling data for a 43.5 bar crystal (Crystal_Nov27_2009_43.5 bar_ initial cooling). It was cooled from 750 mK to the base temperature. The limiting low temperature pressure (P_1) of this crystal at one end is 43.3804 bar. Data from

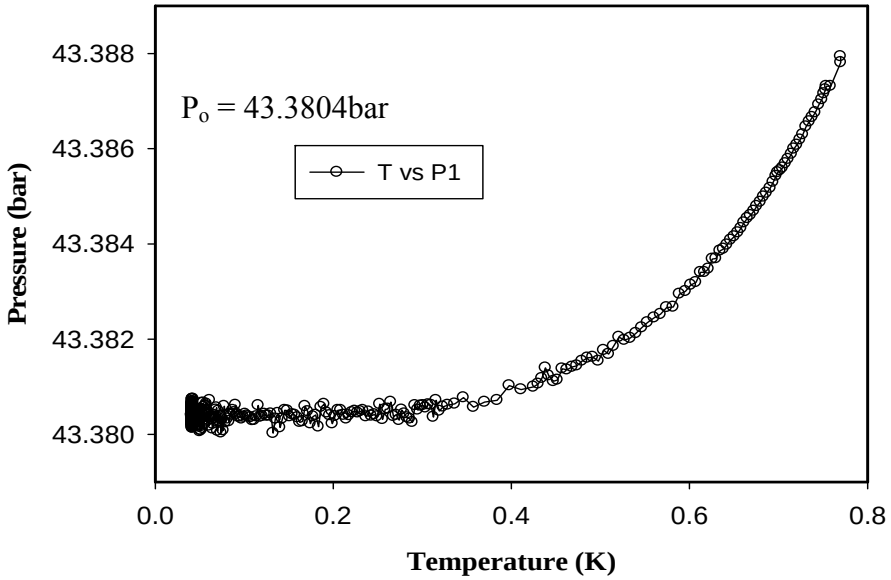

Figure 4.23: Pressure (P_1) at one end shows the initial cooling of crystal (Crystal_Nov27_2009_43.5 bar_750 mJ_ initial cooling) from 750 mK to base temperature.

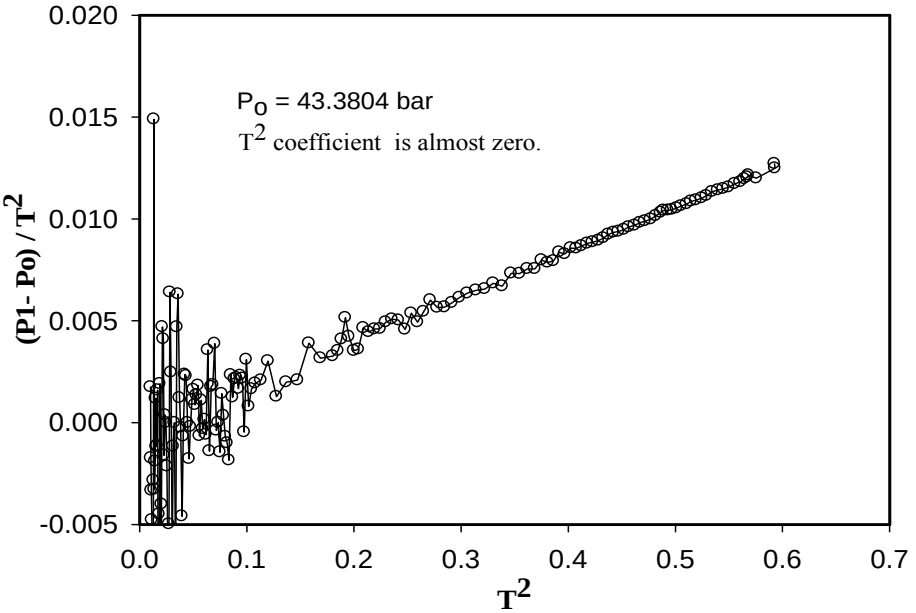

Figure 4.24: Pressure temperature dependence plot illustrates the phonon (Debye) and linear (glass) contribution of the crystal's (Crystal_Nov27_2009_43.5 bar_750 mJ_ initial cooling) pressure (internal heater). Almost zero quadratic contribution is observed.

Figure 4.23 can be used to compare to equation 2.14 (chapter 2) to look for a glassy (T^2) contribution for this crystal. Figure 4.24 plots $(P_1-P_o)/T^2$ vs. T^2. The zero intercept on the vertical axis of the curve indicates the absence of the T^2 term expected for a disordered system. This plot uses data in the temperature range 100 to 750 mK. A measure of the T^4 (Debye) term in the system's pressure is available from this plot but any T^2 term is too small to resolve. Earlier annealing data showed that the annealing of crystal started at a temperature around 500 mK.

We therefore warmed the crystal to higher temperature and then re-cooled to look for a T^2 term. The crystal (Crystal_Nov27_2009_43.5 bar_750 mJ_ annealed) was warmed to 900 mK and then cooled back to the base temperature. Figure 4.25 shows the $(P_1-P_o)/T^2$ vs. T^2 plot for both the warming and the cooling. The plot covers the temperature range 200 to 900 mK. The pressure during cooling is slightly lower than during warming, by about 0.0007 bar/K^2 in the temperature range above 400 mK. This shift, shown in Figure 4.25 is comparable to the scatter in our data below 400 mK so we do not have any clear evidence of a changing glassy T^2 term in the pressure for this crystal.

Some recent experiments found evidence of a glassy T^2 term [6, 7, 49]. Its absence in our measurement might be related to the sensitivity of our strain gauges. Our strain gauges are not very sensitive at low temperature. However we did see evidence of a T^2 term in the case of one crystal (once only) out of the six we have studied. This is shown in Figure 4.26 for the 30.5 bar crystal (Crystal_July24_2009_30.5 bar_ heat pulsed) over the temperature range 150 to

500 mK. The value of the glassy (TLS) T^2 coefficient observed is $A_{TLS} = 0.0018$ bar/K^2. This is comparable to the value 0.002 bar/K^2 obtained in other experiments [6, 7, 49]. This data may be reliable since it is made in a temperature range where we have not seen significant annealing. However, this behavior was not seen in any other crystal in our experiment.

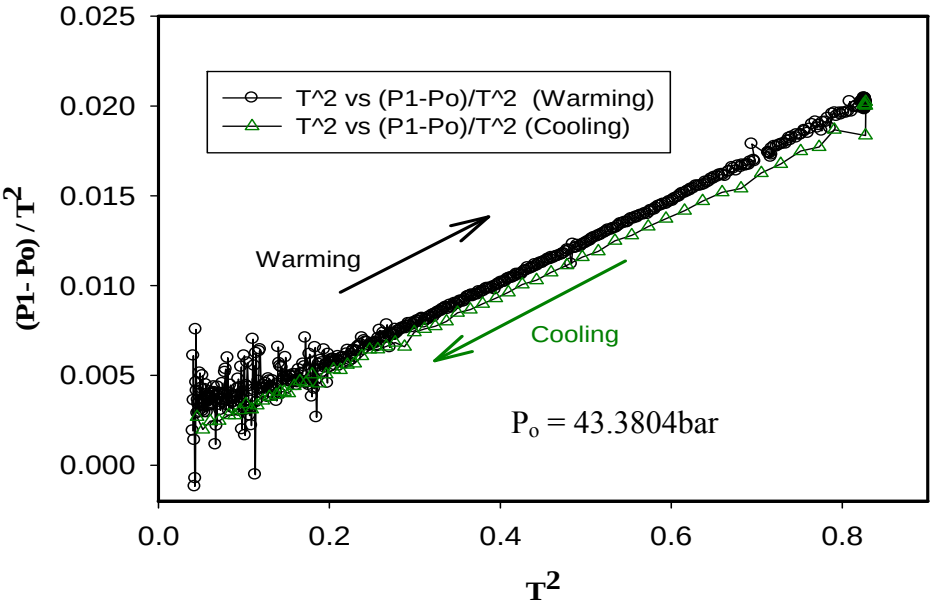

Figure 4.25: Pressure temperature dependence curve in the case of warming and cooling of a crystal (Crystal_Nov27_2009_43.5 bar_750 mJ_ annealed) is plotted. First the crystal is warmed and then cooled. Both show similar characteristics except the 0.0007 bar-K^{-2} drop in the cooling curve.

Some of our other P(T) measurements gave unexpected results. In the case of the 43.5 bar crystal shown in Figure 4.25, a pressure difference of 240 mbar was introduced in this crystal with a 750 mJ heat pulse and the crystal was subsequently ramped to 1.5 K and then cooled to the base temperature. Figure 4.27 shows a plot of $(P_2-P_o)/T^2$ vs. T^2 for both warming and cooling of this crystal.

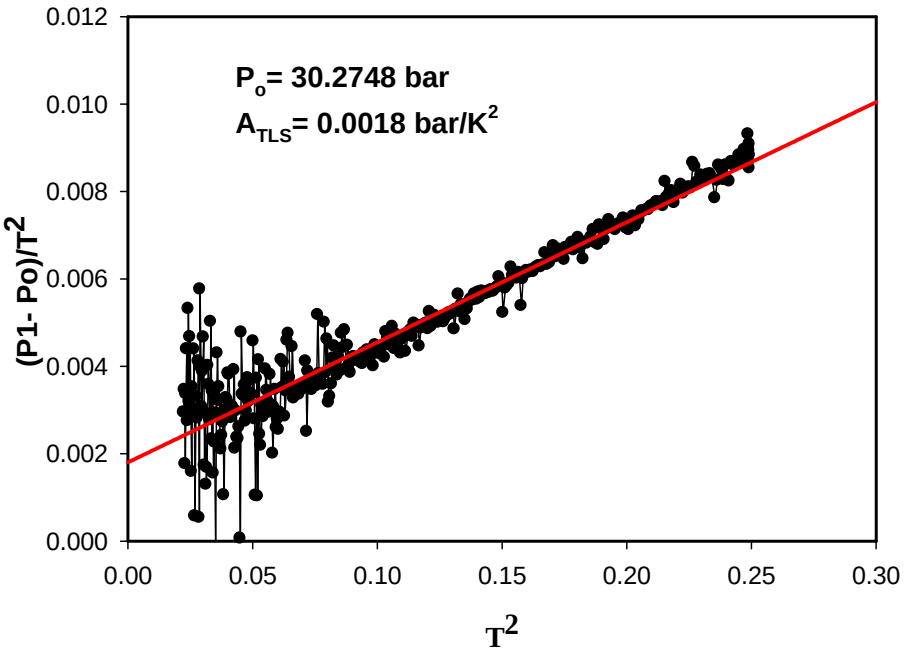

Figure 4.26: Only data (external heater) in our experiment showing a T^2 contribution along with a phonon T^4 term. This is obtained for a 30.5 bar crystal (Crystal_July24_2009_30.5 bar_ heat pulsed). The coefficient of the T^2 term calculated in this case is 0.0018 bar/K^2. The line is a best fit in the temperature range 150 – 500 mK.

Neither the pressure during warming nor during cooling shows a clear intercept (T^2 term) on the vertical axis (Figure 4.27). Warming to 1.5 K caused some annealing, which has been shown to reduce the T^2 term in P(T). However, annealing changes the slope of the P(T) curve (the magnitude of the T^4 term) for this crystal. This result is surprising since annealing should not affect the Debye (T^4) heat capacity term. To give a better look at this effect, we plot (Figure 4.28) the P(T) behavior at the other end (P_1) of the crystal for this measurement. The pressure at this end of the crystal also shows zero intercept (T^2 term) but the slope (T^4 term) is identical for both warming and cooling.

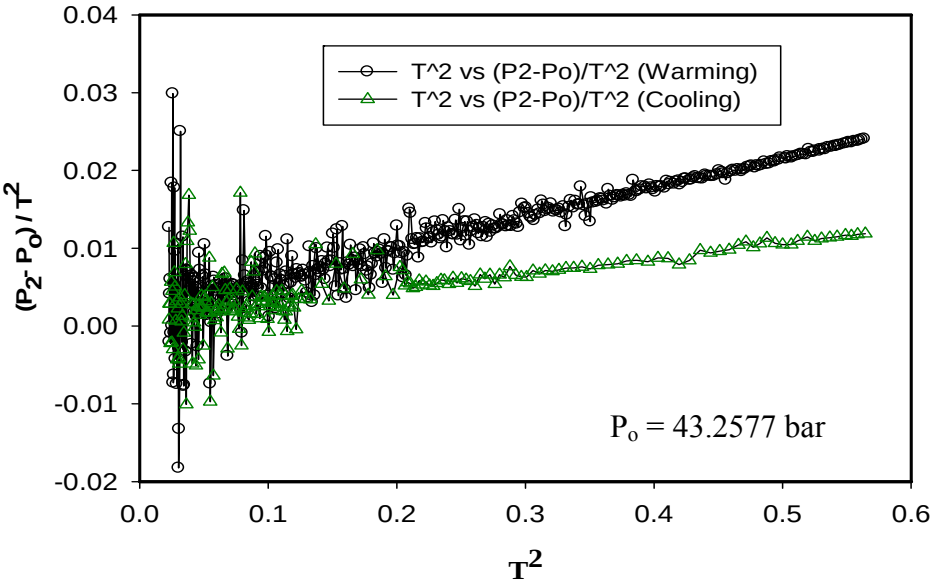

Figure 4.27: Pressure temperature dependence curve (P_2 end) in the case of non-annealed (circle) and annealed (upward triangle) crystal (Crystal_Nov27_2009_43.5 bar_750 mJ_ annealed) is plotted. Annealing (internal heater) affects the phonon contribution but still no sign of a linear contribution is observed.

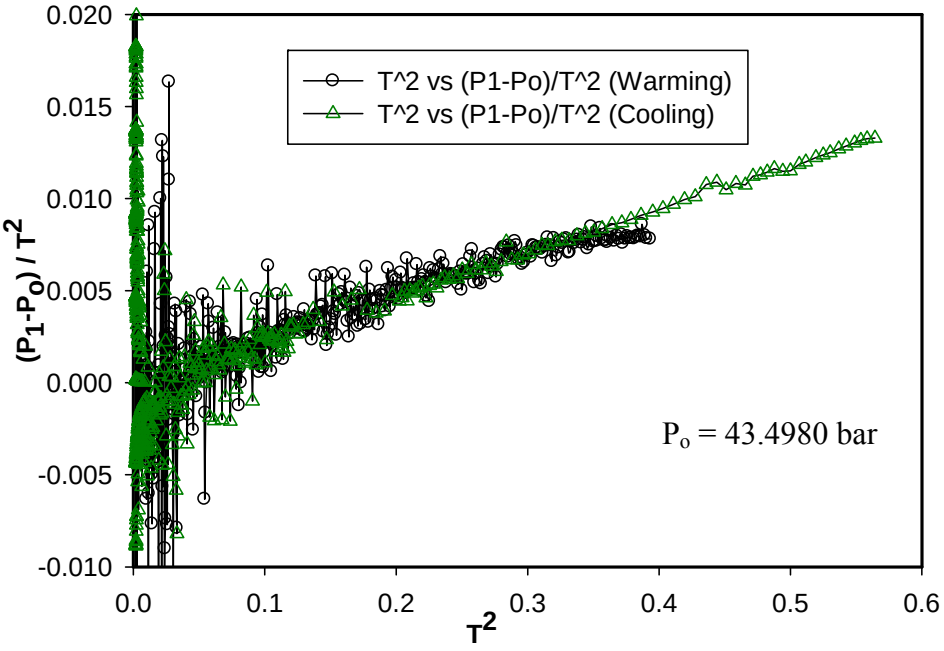

Figure 4.28: Pressure temperature dependence curve (P_1 end) in the case of non-annealed (circle) and annealed (upward triangle) crystal (Crystal_Nov27_2009_43.5 bar_750 mJ_ annealed) is plotted. Annealing (internal heater) does not affect the warming and cooling behavior and no sign of a linear contribution is observed.

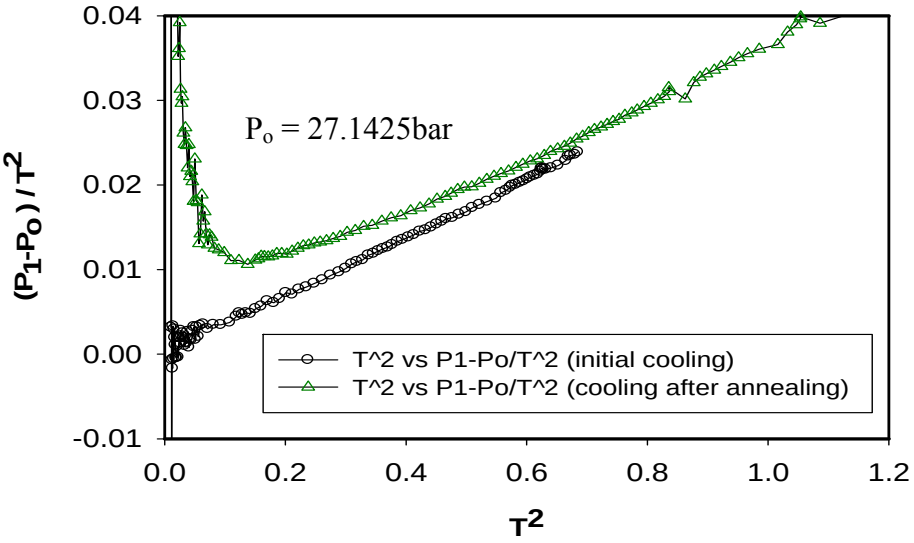

Figure 4.29: T^2 plot (P_1 end) for initial cooling and cooling after annealing (internal heater) in the case of a 28.5 bar crystal (Crystal_Dec07_2009_28.5 bar_ initial cooling). Surprisingly the T^2 curve goes up after annealing.

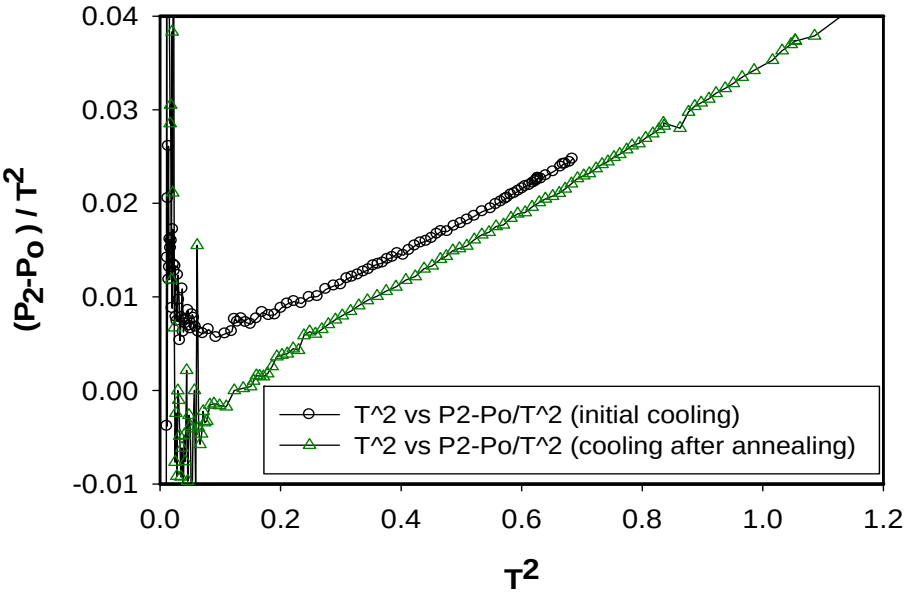

Figure 4.30: T^2 plot (P_2 end) for initial cooling and cooling after annealing (internal heater) in the case of a 28.5 bar crystal (Crystal_Dec07_2009_28.5 bar_ initial cooling). Surprisingly the T^2 curve for cooling at the P_2 end (goes down) is completely different than at the P_1 end in Figure 4.29.

Another interesting P(T) characteristic is seen in a low pressure crystal (Crystal_Dec07_2009_28.5 bar_ initial cooling). After initial cooling, this crystal was annealed for 40 hours up to 1.1 K and then it was cooled to base temperature again. The pressure at one end of this 28.5 bar crystal (P_1) goes up at low temperature due to annealing. This shift in P(T) is shown in the $(P_1-P_o)/T2$ vs. T^2 curve in Figure 4.29. This strange behavior has not been described by other groups [6, 49]. However, the pressure at the other end (P_2) of this crystal shows quite different behavior. Strangely, P_2 shows (Figure 4.30) almost the same behavior as P_1 during initial cooling but decreases after annealing. Here, annealing results in a rise in the crystal's pressure at one end (P_1) and drop in the other end (P_2). This confusing behavior in the crystal's pressure shows that the pressure in a crystal is not uniform and may have different temperature dependences in different regions.

It is clear from our measurements that determining the equilibrium temperature dependence of the pressure in a poly-crystal is very difficult at low temperature due to the non-uniformity in pressure. Moreover, there can be significant temperature and time dependences of pressure in a poly-crystal at low temperature. Thus, despite having an open cell geometry, we have been unsuccessful in determining any reliable glassy (T^2 term) coefficient in our solid ^{4}He crystal. In the case of a more confined geometries [6, 7, 49], we expect large pressure gradients in the crystal, which will make P(T) measurements more difficult. In the case of a well annealed crystal the value of P(T) may be reliable, but this does not allow us to study highly disordered crystals, since annealing

reduces defect densities. Thus more careful experiments are needed to determine the temperature dependence of the pressure in solid ^{4}He.

There may be a T^2 term present in the pressure of solid ^{4}He crystals as observed in some experiments. Our experimental data do not allow us draw any conclusions about its presence or absence. However, we have demonstrated the difficulties in determining such a T^2 contribution in the case of disordered solid ^{4}He crystal, due to the temperature and time dependence of pressure. This also prevents us from calculating a Gruneisen parameter using equation 2.15 and comparing to possible linear terms in heat capacity measurements.

Chapter 5

Conclusion

In this thesis we have used pressure measurements to study the low temperature characteristics of solid ^{4}He crystals and the effects of defects. We have been able to quench cool our sample in around 15 seconds with the use of a weak thermal link between the sample cell and the mixing chamber. This gave us the opportunity to study crystals with high defect densities. In this chapter, we summarize our main experimental results.

We have learned that blocked capillary crystal growth, the bcc/hcp phase transition, thermal quenching and partial melting all introduce pressure gradients in a solid ^{4}He crystal. These pressure gradients stay in a crystal unless they are annealed at a temperature close to the melting point for a long period; even then some pressure gradients will remain in the crystal. The value of the yield stress for our solid ^{4}He crystal was estimated from the maximum pressure gradients as 100 mbar. After reaching this maximum stress, additional thermal quenching does not increase the crystal's pressure gradient.

Annealing reduces the pressure gradients in a crystal. During annealing, pressure does not change uniformly throughout the crystal. Our pressure measurement at the two opposite ends of the cell exhibit different responses to annealing showing that pressure measurements made with a single strain gauge might not correspond to the actual pressure of the crystal. Two or more pressure

gauges are needed to characterize pressure changes in a crystal. Even then, it may not be possible to measure the equilibrium thermodynamic pressure.

Pressure measurements during annealing give the activation energy of the thermal process that governs the annealing. The obtained value of the activation energy (5 K) suggests that thermal vacancies are a possible mechanism for annealing of pressure gradients.

The measurements made on the solid ^{4}He crystal illustrated the dependence of pressure on temperature as well as on time. In addition, P(T) measurements of the two Straty-Adams gauges made on opposite ends of a crystal showed different behavior. Thus, the time and temperature dependence of pressure and the inaccuracy in determining the crystal's pressure with a single pressure gauge limit usefulness of the P(T) and the T^2 (glass) measurements. This limitation restricts the accuracy of the calculation of the Gruneisen parameter for disordered solid ^{4}He crystals. Therefore, the heat capacity estimation using the system's pressure becomes unreliable due to the absence of the Gruneisen parameter value.

The sensitivity of our strain gauges limits our pressure measurements at low temperature. The thermal response time of our thermometers prevents us from getting accurate pressure-temperature measurement during heat pulses and thermal quenching. More sensitive strain gauges and a thermometer placed internally in the solid ^{4}He might improve our pressure-temperature measurements. This would allow the low temperature characteristics of solid ^{4}He to be studied in more detail. The addition of more sensitive gauges might provide more reliable T^2

measurements and make it possible to observe thermal relaxation at low temperature. These improvements could enhance our present understanding of solid helium crystals. Contributions of defects over crystal behavior will then be better understood and then we may be able to interpret supersolid behavior and its mechanism more sensibly.

References

[1] E. Kim and M. H. W. Chan, Nature **427**, 225 (2004).

[2] M. W. Ray and R. B. Hallock, Phys. Rev. B **79**, 224302 (2009).

[3] J. Day and J. Beamish, Nature **450**, 853 (2007).

[4] A.F. Andreev and I.M. Lifshitz, Sov. Phys. JETP 29, 1107 [1969].

[5] Y. Imry and M. Schwartz, J. Low Temp. Phys. **21**, 543 (1975).

[6] V. N. Grigor'ev, V. A. Maidanov, V. Yu. Rubanskii, S. P. Rubets, E. Ya. Rudavskii, A. S. Rybalko, Ye. V. Syrnikov and V. A. Tikhii, Phys. Rev. B **76**, 224524 (2007).

[7] A. S. C. Rittner and J. D. Reppy, J. Phys. Conf. Series **150**, 032089 (2009).

[8] B. Hunt, E. Pratt, V. Gadagkar, M. Yamashita, A. V. Balatsky and J. C. Davis, Science **324**, 632 (2009).

[9] P. W. Anderson, Science **324**, 631 (2009).

[10] C. Enns and S. Hunklinger, Low Temperature Physics, Springer, 2005.

[11] J. Wilks, The Properties of Liquid and Solid Helium, Clarendon Press, Oxford, 1967.

[12] J. R. Beamish, Handbook of Elastic Properties of Solids, Liquids, and Gases, volume 2, Academic Press, San Diego, 2001.

[13] M. Boninsegni, A. B. Kuklov, L. Pollet, N. V. Prokof'ev, B. V. Svistunov and M. Troyer, Phys. Rev. Lett. 99, 035301 (2007).

[14] L. Pollet, M. Boninsegni, A. B. Kuklov, N. V. Prokof'ev, B. V. Svistunov and M. Troyer, Phys. Rev. Lett. 98, 135301 (2007).

[15] M. Boninsegni, N. Prokof'ev and B. Svistunov, Phys. Rev. Lett. 96, 105301 (2006).

[16] E. Kim and M. H. W. Chan, Science 305, 1941 (2004).

[17] A. S. C. Rittner and J. D. Reppy, Phys. Rev. Lett. 98, 175302 (2007).

[18] S. Sasaki, R. Ishiguro, F. Caupin, H. J. Maris and S. Balibar, Science 313, 1098 (2006).

[19] L. Pollet, M. Boninsegni, A. B. Kuklov, N. V. Prokof'ev, B. V. Svistunov, and M. Troyer, Phys. Rev. Lett. 101, 097202 (2008).

[20] D. E. Galli, M. Rossi, and L. Reatto, Phys. Rev. B 71, 140506 (2005).

[21] X. Lin, A. C. Clark, Z. G. Cheng and M. H. W. Chan, Phys. Rev. Lett. 102, 125302 (2009).

[22] J. T. West, O. Syshchenko, J. Beamish and M. H. W. Chan, Nature Physics 5, 598 (2009).

[23] S. Sasaki, F. Caupin and S. Balibar, J. Low Temp. Phys. 153, 43 (2008).

[24] M. W. Ray and R. B. Hallock, Phys. Rev. Lett. 100, 235301 (2008).

[25] H. Suzuki, J. Phys. Soc. Japan 35, 1472 (1973).

[26] A. C. Clark and M. H. W. Chan, J. Low Temp. Phys. 138, 853 (2005).

[27] B. Hébral, G. Frossati, H. Godfrin, D. Thoulouze and A.S. Greenberg In: H.J. Maris, Editor, Phonon scattering in condensed matter, Plenum, New York, 169 (1980).

[28] S. H. Castles and E. D. Adams, J. Low Temp. Phys. 19, 397 (1975).

[29] X. Lin, A. C. Clark and M. H. W. Chan, Nature 449, 1025 (2007).

[30] P. Phillips and A. V. Balatsky, Science 316, 1435 (2007).

[31] J. J. Su, M. J. Graf and A. V. Balatsky, J. Low Temp. Phys. 159, 431 (2010).

[32] D. A. Ackerman, A. C. Anderson, E. J. Cotts, J. N. Dobbs, W. M. MacDonald and F. J. Walker, Phys. Rev. B 29, 966 (1984).

[33] J. R. Beamish, N. Mulders, A. Hikata and C. Elbaum, Phys. Rev. B 44, 17, 9314 (1991).

[34] http://www.lakeshore.com/pdf_files/sensors/LSTC_Germanium_l.pdf

[35] G. C. Straty and E. D. Adams, Rev. Sci. Inst. 40, 1393 (1969).

[36] D. W. Greywall, Phys. Rev. A 3, 2106 (1971).

[37] E. Rolley et al., J. low Temp. Phys. 99, 851(1995).

[38] J. T. Folinsbee and A. C. Anderson, Phys. Rev. Lett. 31, 1580 (1973).

[39] O. V. Lounasmaa, Experimental Principles and Methods Below 1 K, Academic Press, London and New York, 1974.

[40] N. W. Ashcroft, N. D. Mermin, Solid State Physics, Saunders College, Philadelphia, 1976.

[41] G. K. White, P. J. Meeson, Experimental Techniques in Low-Temperature Physics, Clarendon Press, Oxford, 2002.

[42] A. S. Rittner, The impact of disorder on supersolidity on solid helium-4, PhD thesis, Cornell University, 2008.

[43] O. Syshchenko, J. Day and J. Beamish, Phys. Rev. Lett. 104, 195301 (2010).

[44] T. Mizusaki, Y. Hirayoshi, S. Maekawa and A. Hirai, Phys. Lett. A 50, 165 (1974).

[45] B. A. Fraass, P. R. Granfors and R. O. Simmons, Phys. Rev. B 39, 124 (1989).

[46] E. Blackburn, J. Goodkind, S.K. Sinha, C. Broholm, J. Copley and R. Erwin, J. Phys. 71, 673 (2008).

[47] M. Boninsegni, A. B. Kuklov, L. Pollet, N.V. Prokof'ev, B.V. Svistunov and M. Troyer, PRL 97, 080401 (2006).

[48] Y. O. Vekhov,V. N. Grigor'ev, V. A. Maidanov, N. P. Mikhin, V. Y. Rubanskiy, S. P. Rubets, E. Y. Rudavskii, A. S. Rybalko, Y. V. Syrnikov, and V. A. Tikhiy, Low Temp. Phys. 33, 635 (2007).

[49] V. N. Grigor'ev, V. A. Maidanov, V. Yu. Rubanskii, S. P. Rubets, E. Ya. Rudavskii, A. S. Rybalko and V. A. Tikhii, Low Temp. Phys. 34, 344 (2008).